SLX4 assembles nuclear condensates that compartmentalize the SUMO-RNF4 pathway and drive DNA repair

Emile Alghoul, Matteo Paloni, Arato Takedachi, Serge Urbach, Alessandro Barducci, Pierre-Henri Léon Gaillard, Jihane Basbous, Angelos Constantinou

SLX4 assembles nuclear condensates that compartmentalize the SUMO-RNF4 pathway and drive DNA repair.

Emile ALGHOUL[1], Matteo PALONI[2], Arato TAKEDACHI[3], Serge URBACH[4,5], Alessandro BARDUCCI[2], Pierre-Henri GAILLARD[3], Jihane BASBOUS[1*] and Angelos CONSTANTINOU[1*]

1. Institut de Génétique Humaine, Université de Montpellier - CNRS, Montpellier, France
2. Centre de Biologie Structurale (CBS), Université de Montpellier, CNRS, INSERM, Montpellier, France.
3. Centre de Recherche en Cancérologie de Marseille, CRCM, Inserm, CNRS, Aix-Marseille Université, Institut Paoli-Calmettes, Marseille, France.
4. Institut de Génomique Fonctionnelle, Université de Montpellier - CNRS - INSERM, Montpellier, France
5. Montpellier RIO Imaging

* corresponding authors

Short title: SLX4 condensates control the SUMO-RNF4 pathway

Abstract

SLX4 disabled in Fanconi anemia group P is a multifunctional scaffold protein that coordinates the action of structure-specific endonucleases and other DNA repair proteins to ensure genome stability. We show here that SLX4 drives the regulated assembly of an extensive protein network cross-linked by SLX4 dimerization and SUMO-SIM interactions that yield liquid-like nuclear condensates. SLX4 condensates compartmentalize the SUMO system and the STUbL RNF4 to enhance selectively the modification of substrate proteins by SUMO and ubiquitin. Specifically, we find that the assembly of SLX4 condensates induces the processing of topoisomerase 1 - DNA protein crosslinks (TOP1cc), as well as the resection of newly synthesized DNA. This unanticipated function of SLX4 emerges from the collective behavior of proteins that compose SLX4 condensates in live cells. We conclude that SLX4 foci are functional compartments maintained by site-specific protein-protein interactions that control key biochemical reactions in DNA repair.

Introduction

In response to chemical alterations in the primary structure of DNA, hundreds to thousands copies of DNA damage response (DDR) proteins typically accumulate within nuclear foci. DDR foci conform to the definition of biomolecular condensates on the basis that these structures concentrate proteins and nucleic acids without defined stoichiometry and in absence of a surrounding membrane (*1*–*6*). The spatiotemporal organization of biochemical pathways within biomolecular condensates often regulates enzymatic activities and multistep reactions (*7*, *8*).

The mechanisms of assembly of DDR foci and the biological pathways that take place within DDR foci, however, remain largely elusive. Biomolecular condensates are increasingly assimilated to products of liquid-liquid phase separation (LLPS), a structure-independent thermodynamic process determined by the multitude of factors that influence protein solubility (*5*, *9*, *10*). LLPS occurs above saturation concentration of the phase separating protein(s) to achieve thermodynamic stability via spontaneous de-mixing of the system into coexisting phases (*10*–*12*).

The formation of DDR foci, however, is primarily governed by a network of protein - protein interactions, as revealed by interdependencies in protein recruitments through site-specific interactions (*13*). Protein clustering is often driven by a few key multivalent scaffolds that are highly connected to other molecules (Espinosa et al., 2020; Guillén-Boixet et al., 2020; Sanders et al., 2020). A localization-induction model suggests that posttranslational modifications that increase attractive interactions trigger a transition towards the formation of stimuli-responsive condensates (*20*). Consistent with this, protein group modification by SUMO stabilizes protein interactions enhancing biochemical reactions, as exemplified in homologous recombination and ATR activation (*21*, *22*). Likewise, SUMO-SIM interactions stabilize PML nuclear bodies (*23*–*26*).

To gain insights into the assembly mechanisms of DDR foci and the functional relevance of the resulting biomolecular condensates, here we report on the study of SLX4, a low abundant protein scaffold required for genome integrity. Biallelic inactivation of *SLX4* underlies complementation group P of Fanconi anemia (*27*, *28*), an inherited disease associated with congenital abnormalities,

pancytopenia and cancer proneness (*29*). SLX4 associates with multiple DNA repair factors including the structure-specific endonucleases (SSEs) XPF-ERCC1, MUS81-EME1, and SLX1 to repair inter-strand DNA crosslinks, drive the resolution of Holliday junctions, promote DNA repair synthesis at common fragile sites and/or ensure telomere maintenance (*30–40*). Furthermore, SLX4-XPF promotes homologous recombination at a replication fork barrier caused by tightly DNA-bound proteins (*41*). Consistent with this, SLX4-XPF functions upstream of the cellular response to a DNA-protein replication barrier, promoting the recruitment of DNA damage response factors (*42*). Cells defective for SLX4-XPF are hypersensitive to trapped DNA methyltransferases and trapped DNA topoisomerase 1 (*41*, *43*), suggesting that SLX4-XPF are necessary for the repair of some forms of DNA -protein crosslinks (DPCs). How mechanistically SLX4-XPF promotes the processing of tightly DNA bound proteins has yet to be explored.

Here we report that SLX4 drives the formation of biomolecular condensates that compartmentalizes the SUMO/ubiquitination system. We find that SUMO-SIMs interactions and SLX4 dimerization stabilize SLX4 condensates, highlighting the critical role of site-specific interactions. We provide evidence that SLX4 condensates are functional entities that enhance selectively the modification of substrate proteins by SUMO and ubiquitin. We report that the condensation of SLX4 *per se* induces the repair of topoisomerase 1 - DNA crosslinks and the resection of nascent DNA. The data indicate that SLX4 foci are functional condensates assembled through site-specific interactions to control the localization and the timing of biochemical reactions required for the maintenance of chromosome stability.

Results

SLX4 is a major scaffolding component of subnuclear compartments

The recruitment of key protein scaffolds to DNA lesions through specific interactions drive the assembly of DNA damage-induced nuclear foci (*1*). Here we took advantage of a cryptochrome 2

(Cry2) – based optogenetic tool to dissect mechanistically the behavior of SLX4 in live cells. Cry2 forms tetramers upon exposure to 488 nm light (*44*). Fused to a multivalent protein scaffold that underpins the formation of nuclear foci, this optogenetic module offers unprecedented spatiotemporal control over the formation of DDR foci, in the absence of exogenous sources of DNA damage (*3*, *4*). Thus, we fused SLX4 to Cry2 and mCherry to visualize directly the contribution of SLX4 to the formation of nuclear foci in live cells (Figure 1A). We stably integrated the optogenetic SLX4 construct (optoSLX4) in HEK293 cells using FlpIn reaction and expressed the optoSLX4 recombinant protein to near endogenous levels under the control of doxycycline. Exposure of these cells to 4 seconds (4s) cycles of light-10 seconds (10s) resting for three minutes readily induced the formation of multiple SLX4 foci per nucleus, in absence of exogenous sources of DNA damage (Figure 1B). Time-lapse microscopy revealed that optogenetic SLX4 foci are detectable as early as 30 seconds after light exposure and coalesce occasionally (Figure 1C, Video S1, S2, S3). The liquid-like properties of SLX4 foci indicate that these structures are held together by weak interactions that allow rapid exchanges of molecules. SLX4 foci induced by optogenetic activation were reversible. The foci dissolved progressively 20 to 30 minutes after activation (Figure 1D). In absence of optogenetic activation, the formation of spontaneous SLX4 foci was directly proportional to the level of SLX4 expression induced with doxycycline, until reaching a plateau above 3ng/ml doxycycline (Figure 1E). A mCherry SLX4 construct lacking Cry2 confirmed that Cry2 plays no role in the concentration-dependent assembly of spontaneous SLX4 foci (Figure S1). This crude analysis did not yield evidence for the existence of a concentration saturation threshold that triggers SLX4 condensation (Figure 1E and Figure S1). The data indicate that SLX4 is a multivalent hub protein that underpins the assembly of biomolecular condensates visualized as nuclear foci.

Site-specific interactions drive the biogenesis of SLX4 condensates

Next, we exploited this optogenetic system to actuate SLX4 condensates on demand and identify key molecular determinants of SLX4 condensation. SLX4 is largely unstructured with only a few folded

domains, including the Bric-a-brac Tramtrack and Broad complex (BTB) domain (*45*). We created a series of truncated SLX4 proteins fused to the optogenetic module to gain insights into the domains involved in the assembly of condensates (Figure 2A). Optogenetic activation of the BTB dimerization domain alone did not yield condensates (Figure 2A, B and Figure S2A), but deletion of the BTB domain diminished the capacity of SLX4 to assemble condensates (ΔBTB, Figure 2A, B and Figure S2A). Hence, the BTB domains is required but not sufficient for SLX4 condensation. The intrinsically disordered amino terminal region of SLX4 (IDR1) did not form detectable condensates (Figure 2A, B), however, IDR1 was less stable than WT SLX4 (Figure S2A). IDR1 was more stable in combination with the BTB domain (Figure S2A), yet the IDR1-BTB truncated protein did not form condensates either (Figure 2A, B). By contrast, the intrinsically disordered carboxyl terminal portion of SLX4 (IDR2) exhibited partial capacity to assemble SLX4 condensates (Figure 2A, B, Figure S2A), and the fusion of IDR2 to the BTB stimulated SLX4 condensation further (Figure 2A, B and Figure S2A). Thus, the BTB-IDR2 portion of SLX4 enables the formation of SLX4 condensates by optogenetic activation. IDR2 includes multiple SUMOylation sites as well as three SUMO-interacting motifs (SIMs) that may in principle promote the formation of biomolecular condensates (*46–48*).

To evaluate how the BTB and SIMs domains in SLX4 may contribute to the assembly of nuclear condensates, we first relied on molecular simulations. We modelled SLX4 monomer and BTB-mediated dimers as flexible chains of beads representing individual domains and connected by harmonic springs (Figure 2C), following a recent approach for simulating the condensation of associative biopolymers (*49*). In this framework, specific protein - protein interaction between SUMO and SIM domains is modelled by an attractive potential whereas a strong repulsion between domains of the same type ensures a correct one-to-one binding stoichiometry. Further details are described in the method section. Using this coarse-grained approach, we performed extensive simulations to probe condensate formation (Figure 2D) of SLX4 monomers or dimers with various degrees of SUMOylation. While this minimal model necessarily underestimates the number and diversity of intermolecular interactions that occur in cells, this simulation shed some light on the

molecular determinants of SLX4 assembly. Overall, we observed that BTB-mediated dimerization strongly enhances the condensation of SLX4 independently of the total protein concentration (Figure 2E, F), due to the higher interaction valency of SLX4 dimers. In this model, the degree of SUMOylation of SLX4 chains determined SLX4 assembly in a non-monotonic fashion. Whereas the presence of multiple SUMOylated sites enhanced considerably the formation of SLX4 condensates, this trend was partially reversed when most of the potential SLX4 SUMO sites were SUMOylated (Figure 2E, F and S2B), likely because of the saturation of available SIMs with intramolecular interactions.

To verify the prediction that SLX4 dimerization in combination with SUMO-SIM interactions could drive the assembly of SLX4 condensates, we introduced a phenyl to arginine substitution in the BTB domain that disrupts a key contact required for SLX4 dimerization (*45*). The F708R substitution severely impaired the optogenetic activation of SLX4 condensates (Figure 3A, B). Next, we used a mutant construct in which all the aliphatic acids of SIM 1, 2 and 3 were substituted with alanine (SIM*1,2,3), as described (*50*). Cells expressing the SUMO-interacting dead SLX4 mutant protein did not exhibit SLX4 foci when exposed to 488 nm light (Figure 3A, B). Furthermore, we added NaCl, Sucrose or Sorbitol in the cell culture medium to induce osmotic stress and thereby increase protein concentrations in the nucleoplasm (*51*). This treatment was sufficient to induce the formation of SLX4 condensates, without resorting to optogenetic activation, yet the SLX4-F708R and SLX4-SIM*1,2,3 proteins did not yield condensates under these experimental conditions (Figure S2C, S2D), consistent with the notion that SLX4 dimerization and SUMO-SIM interactions drive the assembly of SLX4 condensates. Furthermore, we pre-incubated cells expressing wild type optoSLX4 with ML-792, an inhibitor of the SUMO activating enzyme, and this treatment blocked the formation of optogenetic SLX4 condensates (Figure 3C and S2E). By contrast, inhibition of the ubiquitin activating enzyme with TAK-243 or the proteasome with MG-132 stabilized SLX4 condensates (Figure 3C and S2E), suggesting that a SUMO-ubiquitin circuitry controls SLX4 condensates, as discussed below. Next, we exposed Fanconi anemia patient derived *SLX4* null cells (FA-P) complemented with WT *SLX4*

cDNA to 1 μM camptothecin (CPT) for one hour, and detected SLX4 foci by immunofluorescence staining. This treatment induced the formation of SLX4 foci (Figure 3D). Consistent with optogenetic SLX4 condensates, pre-incubation of cells with ML-792 blocked the formation of CPT-induced SLX4 foci, whereas TAK-243 and MG-132 markedly increased the number of SLX4 foci induced by CPT (Figure 3D).

The SUMO isopeptidase SENP6 directly regulates the size of PML nuclear bodies acting upon the SUMO modified PML substrate protein (*23*). Likewise, the activity of SUMO proteases may antagonized the condensation of SLX4. Since SLX4 is a main target of SENP6 (*52*), we depleted SENP6 by means of RNA interference to probe its role on the regulation of SLX4 condensation (Figure S2F). Suppression of SENP6 increased the number of both spontaneous and light-induced SLX4 condensates per nucleus (Figures 3E and S2G). By contrast, spontaneous and light-induced SLX4 condensates were reduced in cells transfected with recombinant GFP tagged WT SENP6, whereas transfection of a catalytic dead mutant GFP-SENP6-C1030A had no impact on the condensation of SLX4 (Figures 3F). GFP-SENP6-C1030A co-localized with optogenetic SLX4 condensates, consistent with the recruitment of SENP6 to SLX4 compartments (Figure S2H). By contrast, cells transfected with GFP-SENP6-WT (green) did not exhibit SLX4 condensates (Figure S2H). It is noteworthy that within the same microscopic field, SLX4 condensates (red) were visible only in un-transfected cells that do not emit green fluorescence (Figure S2H). Thus, SUMO-SIM interactions promote the assembly of SLX4 condensates under the control of SENP6.

Localization of optogenetic SLX4 condensates

To test if optogenetic SLX4 condensates assemble in their correct location, we deleted the nucleo-localization signal of SLX4 (Figure S3A). We detected optoSLX4 - ΔNLS both in the cytoplasm and in the nucleoplasm, yet under blue light, optogenetic SLX4 - ΔNLS condensates formed specifically in nuclei (Figure S3A). SLX4 signals remained diffuse in the cytoplasm (Figure S3A), consistent with the notion that specific modifications and interactions in the environment of the nucleoplasm are

required for the assembly of SLX4 condensates. OptoSLX4 was chromatin bound (Figure S3B). Induction of optoSLX4 expression with doxycycline decreased the soluble fraction and increased the chromatin bound fraction of XPF (Figure S3B), revealing the scaffolding function of SLX4. In comparison with wild type optoSLX4, the soluble fraction of the dimerization dead F708R SLX4 mutant protein was higher and its chromatin bound fraction was diminished (Figure S3C). Likewise, mutations of the SIM motifs increased the solubility of SLX4, as did the inhibition of the SUMO activating enzyme with ML-792 (Figure S3C), indicating that SLX4 dimerization and SUMO-SIM interactions stabilize optoSLX4 on chromatin.

Optogenetic SLX4 foci co-localized with endogenous, BRCA1, MDC1, TRF2, PML and RPA32 (Figure S3D). Quantification of overlapping fluorescence signals, however, revealed a wide spectrum of signal overlap, which varied from 10% to 80 % (Figure S3E). We conclude that the composition of SLX4 condensates is subjected to changes, most likely during the cell cycle and depending on specific cellular cues. Thus, we quantified SLX4 condensates induced by optogenetic activation throughout the cell cycle using the fluorescent ubiquitylation-based cell cycle indicator PIP-FUCCI (*53*). Light-induced SLX4 condensates were not only detected in the S and G2/M phases of the cell cycle, but also in the G1 phase, yet to a lesser extent (Figure S3F), consistent with a previous report (*42*). The data thus far suggest that optogenetic SLX4 condensates reconstitute the assembly of SLX4 foci.

SLX4 compartmentalizes the SUMOylation/Ubiquitylation system

To gain insights into the functions that arise specifically from the assembly of SLX4 condensates, we used a biotin proximity labelling approach coupled to mass spectrometry. We fused SLX4 to TurboID, an efficient biotin ligase that biotinylates proximal proteins within minutes (*54*). We performed seven biological replicates and ranked the identified proteins in the order of their intensity Based Absolute Quantification (Figure 4A). We detected SLX4-associated proteins reproducibly, for instance XPF, MUS81, SLX4IP and TopBP1. We also identified SUMO2/3 and the E3 SUMO ligases RanBP2, PIAS1, PIAS4 and ZNF451 (Figure 4A). Furthermore, we identified ubiquitin and the E3

ubiquitin ligases TRIM25 and TRIM33 among abundant SLX4 proximal components. In light of a previous report that the SLX4 complex is associated with a E3 SUMO ligase activity (*50*), the data led us to hypothesize that SLX4 may compartmentalize SUMO and ubiquitin modification enzymes and their protein substrates.

To test if SLX4 condensates concentrate E3 SUMO ligases, we combined the optogenetic and the biotin proximity labelling approach. We fused SLX4 to TurboID at its amino-terminus and to mcherry-Cry2 at its carboxyl terminus (Figure 4B). We exposed cells to blue light for 15 minutes of 4s light-30s resting cycles in the presence of biotin in the cell culture medium, as described (*55*). Next, we lysed cells and isolated biotin-labelled proteins using streptavidin-coated beads. The compartmentalization of SLX4 by optogenetic activation increased significantly the amount of PIAS1, PIAS4 and ZNF451 and of SUMO2/3 labelled in proximity of SLX4 (Figure 4C), indicating that SUMO2/3 and the E3 SUMO ligases accumulate locally within SLX4 condensates. Consistent with the compartmentalization of the SUMOylation machinery by SLX4, we detected by immunofluorescence staining both endogenous and GFP-tagged SUMO1 and SUMO2/3 in SLX4 condensates (Figure 4D), as well as GFP-UBC9 and GFP-PIAS4 (Figure 4D).

To evaluate the impact of the compartmentalization of the SUMOylation machinery by SLX4 on the modification of substrate proteins, we transfected optoSLX4 expressing cells with His-SUMO2/3. We exposed these cells to blue light to induced SLX4 condensation, lysed the cells under denaturing conditions and isolated proteins conjugated to SUMO by metal affinity purification (Figure 5A). Earlier studies have shown that SLX4, XPF, MDC1 and BRCA1 are SUMOylated and that these modifications are important for the DNA damage response (*50*, *56*, *57*). We detected SUMOylated optoSLX4 and XPF one minute after optogenetic induction of SLX4 condensates, and the signals increased thereafter (Figure 5B). The SUMOylation of SLX4 and XPF depended on SLX4 dimerization and on the integrity of the SUMO interaction motifs of SLX4 (Figure 5C), which are necessary for SLX4 condensation. Likewise, the condensation of SLX4 promoted the SUMOylation of MDC1 and BRCA1 (Figure 5D). Furthermore, we identified through a candidate approach endogenous EME1 as a

SUMOylation substrate under the control of SLX4 condensation (Figure 5D). SLX4-driven SUMOylation of EME1 was further supported by ex vivo/in vitro SUMOylation assays (Guervilly et al., 2015), where endogenous EME1 co-immunoprecipitated with recombinant SLX4 underwent extensive SUMOylation *in vitro* (Figure S4A, B).

Protein SUMOylation exerts important roles in the DDR, including the regulation of protein localization and the stabilization of physical interactions (*21*, *58–60*). Furthermore, proteins modified by SUMO can be targeted for ubiquitylation and subsequent proteasomal degradation to accelerate protein turnover at DNA damage sites and enable DNA repair (*59*, *61*, *62*). To test if SLX4 compartmentalizes the SUMO targeted ubiquitin ligase (STUbL) RNF4, we transfected cells with GFP-tagged WT RNF4 or the ubiquitin ligase dead mutant GFP-RNF4-C159A. Accumulation of GFP-RNF4-WT within spontaneous and optogenetic SLX4 compartments was observed only in presence of the proteasome inhibitor MG-132 (Figure S4C). In contrast, the ubiquitin ligase dead mutant GFP-RNF4-C159A accumulated in SLX4 compartments even in absence of proteasome inhibition (Figure S4C). Remarkably, transfection of GFP-RNF4-WT in absence of proteasome inhibition instead markedly reduced the number of optogenetic SLX4 condensates (Figure 5E). This suggests that RNF4-mediated protein ubiquitylation promotes the dissolution of SLX4 condensates. Consistent with this, the depletion of RNF4 by RNA interference increased the yield of light-induced SLX4 condensates (Figure 5F). Furthermore, SLX4 condensation increased the amount of ubiquitylated proteins detected in proximity of SLX4 (Figure S4D), and ubiquitin co-localized with SLX4 condensates (Figure S4E). More specifically, SLX4 condensation readily induced robust ubiquitylation of SLX4 and XPF, as revealed by the immunodetection of proteins purified by metal affinity from cells transfected with His-ubiquitin (Figure 5G).

SLX4 compartmentalization also triggered the ubiquitylation of MDC1 (Figure 5H). By contrast, BRCA1 was not ubiquitylated, consistent with the finding that BRCA1 SUMOylation stimulates its E3 ubiquitin ligase activity (*57*), rather than its degradation by the proteasome. Last, suppression of RNF4 by RNA interference inhibited the ubiquitylation of SLX4, XPF and MDC1 (Figure 5I).

Collectively, the data suggest that SLX4 compartmentalizes and enhances the activity of the E3 SUMO ligases and STUbL RNF4 to modify substrate proteins selectively.

SLX4 condensates enhance the degradation of topoisomerase 1 DNA - protein crosslinks

SUMO-targeted protein ubiquitylation and proteasomal degradation is emerging as a DNA protein crosslinks (DPCs) degradation pathway, as illustrated by the degradation of topoisomerase 1 cleavage complexes (TOP1cc) (*63*), crosslinked DNA (cytosine-5)-methyltransferase 1 (DNMT1) (*64*), and trapped PARP1 (*65*). TOP1cc are modified by the PIAS4/RNF4 system and then degraded by proteolysis (*63*). This pathway is conserved in yeast where the human ortholog of RNF4 is the heterodimer Slx5-Slx8, (*63*). Given the role of SLX4 in the compartmentalization of the SUMO/ubiquitylation system described above, the genetic relationship between *Slx4* and the *Slx5-Slx8* genes (*66*), and the hypersensitivity of SLX4 defective cells to camptothecin (CPT) (*43*, *67*), we assessed the function of SLX4 condensation in the degradation of TOP1cc. The condensation of SLX4 markedly enhanced the conjugation of TOP1 to SUMO and ubiquitin (Figure 6A, upper and middle panels), and depletion of the STUbL RNF4 by RNA interference impaired the ubiquitylation of TOP1 within SLX4 compartments (Figure 6A, bottom panel). We used the DUST assay to assess the contribution of SLX4 condensation in the extraction of DNA-TOP1 protein crosslinks (*63*, *68*). Briefly, we lysed camptothecin treated cells under strong denaturing conditions to disrupt non-covalent interactions. Next, we purified DNA along with crosslinked proteins and probed TOP1-DPCs by immunoblotting. We isolated TOP1-DPCs from cells treated with camptothecin for 15 minutes (Figure 6B). Optogenetic activation of SLX4 condensates with 488 nm light pulses at the 5-minute and 10-minute time points during CPT treatment reduced the amount of TOP1-DPCs isolated from these cells (Figure 6B). Consistent with a function for SLX4 in the degradation of TOP1 covalently linked to DNA, immunodetection of TOP1cc by fluorescence microscopy revealed high levels of DNA-TOP1 crosslinks in Fanconi anemia patient derived *SLX4* null cells exposed to camptothecin (Figure 6C, D). Complementation of these cells with WT *SLX4* cDNA reduced significantly the level of TOP1cc

signals (Figure 6C, D). Furthermore, doxycycline-induced expression of recombinant SLX4 in HEK293 cells reduced the camptothecin-induced TOP1cc signal (Figure 6E, F). Collectively, the data indicate that compartmentalization of the SUMO/ubiquitylation system within SLX4 condensates promotes the extraction of TOP1 DNA-protein crosslinks from chromatin.

SLX4 condensation induces the degradation of newly replicated DNA

The data so far suggest that the condensation of SLX4 enhances the SUMOylation and SUMO-dependent ubiquitylation of substrate proteins. Considering that this system likely amplifies endogenous processes that would normally occur under specific and highly regulated circumstances, we probed the consequences of SLX4 condensation on replication fork collapse, a process that normally occurs as a last resort when obstacles to the progression of replication forks persist (*42*, *50*, *69*, *70*). Replication fork collapse can be defined as the dissociation of replisome components (*71*). In mammalian cells, the collapse of replication forks is driven by the SUMOylation and SUMO-targeted ubiquitylation of replisome components in a manner that depends on the combined action of RNF4, the AURKA-PLK1 pathway and SLX4 (*72*). We used a DNA fiber labeling approach to assess directly the impact of SLX4 condensation on DNA replication. We labelled cells with two consecutive pulses of iododeoxyuridine (IdU) and chlorodeoxyuridine (CldU) for 30 minutes each, and then exposed the cells for 3 minutes to blue light every 30 minutes for 2 hours (Figure 7A). Since optogenetic SLX4 compartments dissolve spontaneously 30 minutes after induction (Figure 1D), this experimental procedure ensures the presence of SLX4 condensates for two hours. Replication forks progress normally at constant speed, hence the ratio of CldU/IdU replication track length is close to one (Figure 7B). After optogenetic activation of SLX4 condensates, however, the length of CldU replication tracks were shorter than IdU replication tracks (Figure 7B). By contrast, the ratio of CldU/IdU replication tracks remained close to 1 in cells expressing the dimerization or SUMO interacting defective mutants F708R SLX4 and SIM*1,2,3, respectively (Figure 7B). Consistent with this, the ratio of CldU/IdU replication tracks was unaffected by 488 nm light in cells treated with the

SAE inhibitor ML-792 (Figure 7C). Thus far, the data suggest that in absence of inhibitors of DNA replication, SLX4 condensation either promotes the degradation of CldU-labelled DNA, or induces the stalling of DNA replication forks. Depletion of RNF4 by RNA interference, however, blocked the shortening of CldU - labelled replication tracks (Figure 7D). In this context, the degradation of nascent DNA is expected to be initiated by SLX4-associated SSEs. Biotin-proximity labeling confirmed that endogenous MUS81, EME1, XPF, and ERCC1 were associated with optoSLX4 (Figure S5A). GFP tagged MUS81, GFP tagged SLX1 and endogenous XPF co-localized with optogenetic SLX4 condensates (Figure S5B, C, D). To verify the contribution of the SSEs to nascent DNA degradation, we used an optoSLX4-SMX* mutant protein that is unable to interact with any of the three SSEs (*73*). Light-induced compartmentalization of optoSLX4- SMX* did not induce significant degradation of CldU-labelled replication tracks (Figure 7E), despite the possible presence of endogenous SLX4 in optogenetic SLX4 compartments that would in principle offer binding sites for SSEs. Control experiments confirmed that optoSLX4-SMX* formed light-induced condensates (Figure S5E, F). In fact, the latter where more numerous and bigger than wild-type optoSLX4 condensates. As expected, cellular treatment with the MRE11 inhibitor Mirin also blocked the degradation of nascent DNA (Figure 7F), without affecting the formation of SLX4 condensates (Figure S5G, H, I). Furthermore, the condensation of SLX4 induced the progressive accumulation of RAD51 foci (Figure 7G, H). Altogether, the data indicates that SLX4 condensates promote a cascade of biochemical reactions including protein modifications with SUMO and ubiquitin and nucleolytic reactions leading to the degradation of nascent DNA and the recruitment

of the recombinase RAD51.

Discussion

This study suggests a mechanistic paradigm for understanding how a hub protein orchestrates DNA repair through the assembly of reversible compartments with defined composition and functions at DNA damage sites. SLX4 binds specifically to partner proteins and forms protein complexes with defined stoichiometry and functional properties that can be reconstituted *in vitro* (*35*, *36*, *74*). Here we show that in the nucleus, the multivalent SLX4 scaffold oligomerizes extensively via SUMO-SIM and homotypic BTB interactions to yield an extensive, non-stoichiometric protein network visualized as a nuclear focus by conventional microscopy (Figure 7). The composition of SLX4 condensates is most likely determined by the combination of SLX4 specific protein-binding interfaces as well as accessible SUMO conjugates that provide a platform for the recruitment of SIM-containing client proteins (*47*). Optogenetic control of SLX4 condensation with high temporal precision revealed that SLX4 condensates concentrate enzymes implicated in protein modification by SUMO and ubiquitin, and amplify the modification of substrate proteins. The enhancement of protein modification most likely results from the local concentration of enzymes and substrates within SLX4 condensates, which favors protein rebinding after dissociation, that is, the overall binding avidities (*75*). Consistent with this, SUMOylation rates are increased up to more than 30 folds when the SUMOylation machinery is localized in the confined space of an engineered condensate (*76*).

We obtained evidence that SENP6 and RNF4 regulate the formation and the dissolution of SLX4 condensates, respectively. The SUMO -specific peptidase SENP6 controlled the level of SLX4 sumoylation, which determined directly the efficacy of SLX4 condensation. Once formed, SLX4 condensates primed their dissolution via RNF4-mediated SLX4 ubiquitylation, suggesting a negative feedback mechanism for the containment of protein modification in time.

Among SLX4 protein substrates, we identified topoisomerase 1-cleavage complexes. Thus, in addition to the control of endonuclease reactions, we provide evidence that SLX4 promotes the repair of TOP1cc through activation of the SUMO/RNF4 dependent protein degradation pathway (*63*). This unanticipated function of SLX4 emerges from the collective behavior of proteins that

compose SLX4 condensates. The condensation of SLX4 also enhanced the degradation of nascent DNA in absence of exogenous source of DNA replication stress. Nucleolytic processing of replication intermediates is normally prevented by ATR, and is expected to occur only as a last resort mechanism (*77*). The optogenetic system used in this study recapitulates the functions that arise specifically upon assembly of SLX4 condensates, and, therefore, bypasses endogenous mechanisms that regulate the nucleation of SLX4 condensates in the first place. That said, the control of SLX4 condensates by light revealed that SLX4-driven degradation of nascent DNA not only depends on its interaction with the SSEs, but also on the compartmentalization of the E3 SUMO ligases and the STUbL RNF4. This is consistent with an earlier report that the collapse of stalled replication forks depends on SUMOylation and ubiquitylation of replisome components (*72*).

Extensive SUMOylation of DNA replication and DNA repair proteins are necessary for cells to cope with DNA damage (*21*, *58*, *59*), and the SUMO-targeted ubiquitin ligase RNF4 promotes the necessary turnover of proteins at DNA damage sites (*59*, *61*, *62*). Importantly, protein SUMOylation and subsequent SUMO-targeted ubiquitylation defines a pathway for the removal of topoisomerase 1, DNMT1 and PARP1 enzymes trapped on DNA by selective drugs (*63–65*, *68*). The data presented in this study suggest a mechanism for the selective modification of proteins by SUMO and ubiquitin. In this model, compartmentalization of substrate proteins within SLX4 condensates ensures the spatial containment of protein group modifications (*21*), as suggested for PML nuclear bodies (*78*, *79*).

This work suggests that the assembly of SLX4 biomolecular condensates is driven by site-specific protein-protein interactions. High resolution of the underlying SLX4 protein network are necessary to understand how microstructures dictate the composition and the functional properties of SLX4 condensates.

Acknowledgement

We thank Agata Smogorzewska for providing the FA-P (RA3331) cells stably transfected with expressing vector control or SLX4 expressing vector, and Ronald Hay, Stephen Jackson, Stephen West and Orian Amir for providing cDNAs. We acknowledge the national infrastructure France-BioImaging supported by the French National Research Agency (ANR-10-INBS-04). This work was supported by the Fondation ARC pour la recherche sur le cancer (PGA1 RF20180206787), the Fondation MSD AVENIR, by the ANR BioTop project (AAPG2021) of the French Agence Nationale de la Recherche, and by the Labex EPIGENMED, Montpellier, France.

Methods and protocols

- Cell culture and transfections
- Cloning
- Generation of stable cell lines
- Optogenetic activation of SLX4 condensation
- Live imaging
- Fluorescence recovery after photobleaching (FRAP)
- Stimulated emission depletion (STED) microscopy
- Western blot
- Immunofluorescence staining
- TurboID
- Mass spectrometry
- Pulldown of His tagged proteins
- Ex Vivo/In Vitro SUMOylation Assay
- DUST assay
- DNA fiber assay
- Clonogenic assay
- Molecular simulations

Cell culture and transfections

Flp-In™ 293 T-REx and all Flp-In™ 293 T-REx derived stable cell lines were grown under standard sterile cell culture conditions (37˚C, 5% CO_2, humidified incubator) in Dulbecco's modified Eagle's medium (DMEM) containing 10% fetal bovine serum and penicillin-streptomycin. All cells were routinely tested for mycoplasma and scored negative. Parental cells were selected with 100µg/ml Zeocin and Flp-In™ 293 T-REx derived stable cell lines were maintained with 5mg/mL Blasticidin and 50mg/mL Hygromycin B.

Sodium chloride (NaCl) (300mM), sucrose and sorbitol were prepared freshly in DMEM prior to cell treatments. ML-792 (2µM), TAK-243 (2µM) or MG-132 (10µM) were added to the cell culture media for 4 hours prior to Blue light exposure or Mirin (100µM) as indicated in the legend section.
For transient transfections with GFP-tagged constructs (SENP6, SENP6-C1030A, RNF4, RNF4 C159A, MUS81, SLX1) cells were seeded to reach 80% the day of transfection. For 6 well plates, 4µg of cDNA and 8uL Lipofectamine 2000 were used. Media was changed after 6 hours, and cells were assessed for recombinant protein expression after 24 hours. For knockdown experiments, SMARTpool siRNA was acquired from Dharmacon. For each condition, a minimum of 20nM siRNA was transfected using INTERFERin transfection reagent. Knockdown efficiency was assessed 48 hours post-transfection.

Cloning

Primers used for the construction of plasmids are listed in Table S1. For pcDNA5_FRT_TO_optoSLX4-wt, SIM*1,2,3 and SMX, cDNA (a kind gift from Pierre-Henri Gaillard) was amplified with primers 1 and 2 using Phusion High-Fidelity DNA Polymerase. The amplified sequence was inserted in the *KpnI* site of pCDNA5_FRT_TO_TurboID-mCherry-Cry2 (Addgene 166504).
For pcDNA5_FRT_TO_mCherry-SLX4, primers 2 and 3 were used to linearize a mCherry-Cry2 construct, thus deleting Cry2. SLX4 was amplified with primers 5 and 6. Cloning was achieved with the In-Fusion HD Cloning Kit (Takara).
For the structure-function analysis, the vector pCDNA5_FRT_TO_Cry2-NLS-mCherry was prepared by amplifying Cry2 (Primer 9, 10), mCherry (Primer 11, 12), SLX4-NLS (Primer 13, 14), and the pcDNA5 vector (Primer 15, 16). Assembly was made using the In-Fusion HD Cloning Kit. This vector was

linearized with PCR (Primers 17, 18) and used to insert SLX4 fragments using the designated primers (Primer 19-32).
Mutation in SLX4 were generated using the QuickChangeMulti Site-directed mutagenesis kit. F708R with primer 33.
pcDNA5_FRT_TO_Cry2-HaloTag was generated by amplifying HaloTag with primers 44 and 45 which was inserted in the pcDNA5_FRT_TO-Cry2 vector linearized with primers 42 and 43. SLX4 was then amplified with primers 46 and 47 to be inserted in the BsiWI site to generate pcDNA5_FRT_TO_Cry2-SLX4-HaloTag.
pcDNA3-HA-RNF4 wild-type and C159A were obtained as a kind gift from Amir Orian. RNF4 was amplified using primer 50 and 51 to be inserted in pEGFP-C1 linearized with primer 48 and 49.
PBABE-eGFP-MUS81 and SLX1 were generated by amplifying the cDNA with the respective primers 52-55 and inserted in the EcoRI site in the pBABE-puro-eGFP vector.

Generation of stable cell lines
Flp-In™ 293 T-REx cells are seeded to reach 80-90% confluency on the day of transfection. pcDNA5_FRT_TO expression plasmids were mixed with pOG44 encoding the Flp recombinase at a 1:7 ratio in opti-MEM. For a single transfection in a 6 well plate, 500ng of the expression plasmid was mixed with 3.5µg of pOG44 in 250uL opti-MEM. Additionally, 8uL Lipofectamine 2000 transfection reagent was added to 250uL opti-MEM. After an incubation period of 5 min at room temperature, both solutions were mixed and incubated for another 15 min at room temperature. The mix was then pipetted dropwise onto the cells. The medium was replaced after 6 hours. 48 hours post transfection, the cells were transferred to a 100mm petri dish, and 24 hours later, the selection was performed by adding 5mg/mL Blasticidin and 50mg/mL Hygromycin B. Clones were pooled and the cells were tested for the expression of the construct with immunoblotting and fluorescent microscopy.

Optogenetic activation of SLX4 condensation
Cells were plated at around 70% confluency in DMEM. Expression of optoSLX4 was induced for 16 hours with 6ng/ml doxycycline. For light activation, plates were transferred into a custom-made illumination box containing an array of 24 LEDs (488nm) delivering 10mW/cm2. Nucleation was induced using 3 min of light-dark cycles (4 seconds light followed by 10 seconds dark). Images were captured using a 63x objective (NA 1.46 oil). Foci number quantification was done using ImageJ (NIH).

Live imaging
Live imaging of optoSLX4 cells was performed on a DeltaVision OMX V3/V4 microscope (GE Healthcare) equipped with a ×100/1.4 numerical aperture (NA) Plan Super Apochromat oil immersion objective (Olympus). Diode lasers at 488 and 561nm were used to activate the cells and to acquire the mCherry signal respectively. Cells were exposed to 488nm light for 300ms, and z-stacks were acquired with an exposure time of 20ms at a frame rate of 1 image/2 second. All recordings were carried out at 37°C under 5% CO2.

Fluorescence recovery after photobleaching (FRAP)
OptoSLX4 cells were seeded into µ-Dish35 mm, high (Ibidi, 81156) and incubated for 16 hours in the presence of 6ng/ml doxycycline to induce expression of the construct. Imaging was realized using a 63x objective (NA 1.4). SLX4 condensates were photo-bleached and the mCherry signal intensity was measured before and for 5 min following bleaching. A total of 500 images were taken during the 5 minutes. The analysis was done using ImageJ (NIH).

Stimulated emission depletion (STED) microscopy

Flp-In™ 293 T-REx cells expressing Cry2-SLX4-HaloTag were stained with 200nM Janelia Fluor® HaloTag® JF646 for 15 min at 37°C. After 2 washes with a warm medium, cells were activated by light, fixed, and processed for immunostaining with the corresponding partner antibody, and a STAR ORANGE conjugated secondary antibody (Abberior). Confocal and STED imaging was performed using a quad scanning STED microscope (Expert Line, Abberior Instruments, Germany) equipped with a PlanSuperApo 100x/1.40 oil immersion objective (Olympus, Japan). JF646 and Abberior STAR Orange were imaged at 640 and 561nm excitation. Detection was set to 650-750nm for and 570-630nm respectively. A dwell time of 10ms was used. Images were collected in line accumulation mode (5 lines), the pinhole was set to 1.0 Airy units and a pixel size of 10nm was used for all acquisitions.

Western blot

Whole-cell extracts were obtained by lysing the cells in RIPA buffer (50mM Tris, 150mM NaCl, 1% NP-40, 1% Deoxycholate, 0.1% SDS, pH 8) for 30 min on ice. After centrifugation, the supernatant was collected and the amount of proteins was quantified by the Quick Start Bradford protein assay kit. Laemmli buffer was added, and proteins were boiled 5 min at 95 °C. 40µg of protein samples are resolved using pre-cast SDS-PAGE gels (4-15% and 10%) and transferred to a nitrocellulose membrane using the BioRad Trans-Blot Turbo transfer apparatus. Membranes were blocked with 5% non-fat milk diluted in TBS-0.1% Tween 20 (TBS-T), incubated with primary antibodies overnight at 4°C then with anti-mouse or anti-rabbit HRP secondary antibodies for 1 hour. Blots were developed with ECL according to the manufacturer's instructions.

Immunofluorescence staining

For the visualization of optogenetically induced foci, cells expressing the designated constructs are seeded on coverslips and treated as required (Inhibitors, siRNA or cDNA transfection). After light activation, the cells are fixed with PBS/4% paraformaldehyde (PFA) for 15 min at RT followed by a 5 min permeabilization and counterstaining step in PBS/ 0.2% Triton X-100/ 1mg/mL Hoechst 33342.

For immunostaining, cells grown on coverslips were fixed with PFA for 15min at RT followed by a 10min permeabilization step in PBS/ 0.2% Triton X-100-PBS and blocked in PBS/3% BSA for 30min. Primary antibodies and appropriate secondary antibodies coupled to fluorochrome were diluted in blocking solution and incubated for 1h at RT. DNA was stained with Hoechst 33342.

Coverslips were mounted on glass slides with Prolong Gold antifade reagent. Images were captured using a 63x objective (NA 1.46 oil).

For Top1cc immunostaining, cells were seeded on coverslips. After the indicated treatment, cells were fixed with 4% PFA for 15 min on ice, then permeabilized for the same period with PBS/0.25% Triton X-100. Antigens were rendered accessible by a 1% SDS treatment for 5 min. Cells were then washed with wash buffer (PBS/0.1% BSA/0.1% Triton X-100) and blocked using 10% non-fat milk in PBS. The primary antibody (Topoisomerase1-DNA cleavage Complex) was incubated overnight at 1:100 in PBS containing 5% goat serum. After 5 washes with wash buffer the cells were incubated with Alexa Fluor 488-conjugated secondary antibody at 1:1000 in PBS/ 5% goat serum for 1 hour. DNA was then stained with Hoechst 33342 and coverslips were mounted with Prolong Gold antifade reagent.

Pulldown of biotinylated proteins: TurboID

Flp-In™ 293 T-REx cell lines stably transfected with optoSLX4 recombinant protein grown to 75% confluence were incubated with 6ng/ml of doxycycline for 16 hours. Next day, cells were incubated with 500µM of biotin for 10 min. Cells were then washed with PBS and lysed with lysis buffer (50mM Tris-HCl pH 7.5, 150mM NaCl, 1mM EDTA, 1mM EGTA, 1% NP-40, 0.2% SDS, 0.5% Sodium deoxycholate) supplemented with 1X complete protease inhibitor, 1X phosphatase inhibitor and 250U benzonase. Lysed cells were incubated on a rotating wheel for 1 hour at 4°C prior sonication on ice (40% amplitude, 3 cycles 10 sec sonication- 2 sec resting). After 30 min centrifugation (7750

rcf.) at 4°C, the cleared supernatant was transferred to a new tube and total protein concentration was determined by Bradford protein assay. For each condition, 2mg of proteins were incubated with 50µl of Streptavidin-Agarose beads on a rotating wheel at 4°C for 3 hours. After 1min centrifugation (400 rcf.), beads were washed, successively, with 1ml of lysis buffer, 1ml wash buffer 1 (2% SDS in H2O), 1ml wash buffer 2 (0.2% sodium deoxycholate, 1% Triton X-100, 500mM NaCl, 1mM EDTA, and 50mM HEPES pH 7.5), 1ml wash buffer 3 (250mM LiCl, 0.5% NP-40, 0.5% sodium deoxycholate, 1mM EDTA, 500mM NaCl and 10mM Tris pH 8) and 1ml wash buffer 4 (50mM Tris pH 7.5 and 50mM NaCl). Bound proteins were eluted from the agarose beads using 40µl of 2X Laemmli Sample buffer and sent for mass spectrometry analysis. For western blot analysis of SLX4 partners enriched within optogenetic SLX4 condensates, cells were simultaneously incubated with 500µM of biotin and exposed to blue light for 10 min of light-dark cycles (4 sec light followed by 30 sec dark). Biotin proximity labeling of light-induced SLX4 partners were pulled-down using streptavidin-coated beads as described before. Bound proteins were eluted from the agarose beads using 80µl of 2X Laemmli Sample buffer and incubated at 95°C for 10 min. 5µg of the lysates were used for western blot analysis and probed by immunoblotting to detect proteins that are associated with SLX4 clusters, in absence of DNA damage.

Mass spectrometry

Sample digestion was essentially performed as described (Shevchenko et al., 2006). Briefly, proteins were loaded on a SDS-PAGE (BioRad, 456-1034) and, after short migration, a single band was excised. Proteins in the excised band were digested with Trypsin (Promega). The resulting peptides were analyzed online by nano-flow HPLC-nanoelectrospray ionization using a Qexactive HFX mass spectrometer (Thermo Fisher Scientific) coupled to a nano-LC system (Thermo Fisher Scientific, U3000-RSLC). Desalting and preconcentration of samples were performed online on a Pepmap® precolumn (0.3 3 10mm; Fisher Scientific, 164568). A gradient consisting of 0% to 40% B in A (A: 0.1% formic acid (Fisher Scientific, A117), 6% acetonitrile (Fisher Scientific, A955), in H2O (Fisher Scientific, W6), and B: 0.1% formic acid in 80% acetonitrile) for 120 min at 300nl/min was used to elute peptides from the capillary reverse-phase column (0.075 3 250mm, Pepmap®, Fisher Scientific, 164941). Data were acquired using the Xcalibur software (version 4.0). A cycle of one full-scan mass spectrum (375–1,500 m/z) at a resolution of 60000 (at 200 m/z) followed by 12 data-dependent MS/MS spectra (at a resolution of 30000, isolation window 1.2 m/z) was repeated continuously throughout the nanoLC separation. Raw data analysis was performed using the MaxQuant software (version 1.6.10.43) with standard settings. Used database consist of Human entries from Uniprot (reference proteome UniProt 2021_01) and 250 contaminants (MaxQuant contaminant database).

Pulldown of 6xHis tagged SUMO and Ub conjugates

OptoSLX4 cells were seeded in 100mm dishes. 24 hours later, cells were transfected with 6xHis-SUMO2 or 6xHis-Ub. 6 hours post-transfection, doxycycline was added at 6ng/ml to express optoSLX4. The next day, cells were collected after light activation. The cell pellet was directly lysed in denaturing buffer (6M GuHCl, 0.1M NaH2PO4, 10mM TrisHCl pH 8, 5mM β-Mercaptoethanol, 5mM Imidazole). Extracts were briefly sonicated before centrifugation. Cleared extracts were incubated with TALON metal affinity resin for 1 hour at RT. Beads were washed 3 times with denaturing 8M Urea buffer before elution in loading buffer supplemented with 250mM Imidazole. For experiments where knockdown was necessary, siRNA and then cDNA transfections were executed on days 2 and 3 respectively post-seeding.

Ex Vivo/In Vitro SUMOylation Assay

Ex vivo/in vitro SUMOylation assays were performed as described previously in (Guervilly et al. 2015). Briefly, YFP tagged SLX4 complexes were immunoprecipitated from HeLa cell lines stably expressing YFP-SLX4 under the control of a doxycycline-inducible promoter. Cells were washed with

PBS and lysed with NETN buffer (50mM Tris-HCl pH 8.0, 150mM NaCl, 1mM EDTA, 1% NP-40, 1mM DTT, 0.25mM PMSF) containing a proteasome inhibitor cocktail. After centrifugation, supernatants were incubated with a GFP nanobody (provided by M. Modesti) for 2 hours at 4°C. The beads were washed 3 times with NETN buffer, twice with TBS and 5 times with 50mM Tris-HCl pH 8.0. SLX4 complexes immobilized on the beads were then incubated for 60 min at 37°C in a standard reaction mixture containing 50mM Tris-HCl pH 7.6, 10mM MgCl2, 0.2mM CaCl2, 4mM ATP, 1mM DTT, 228nM of E1 (SAE1/UBA2: Boston Biochem), 2.5µM of E2 (Ubc9: Boston Biochem), and 12.5µM of SUMO2 (Boston Biochem).

DUST assay

2 million of optoSLX4 cells were seeded on 60 mm dishes. 24 hours later, cells were incubated with 6ng/ml of Doxycycline for 16 hours. The next day, 1µM of Campthotecin was added to the cells and exposed or not to 1min of light-dark cycles (4 seconds light followed by 10 seconds dark). Cells were lysed in 1ml of M buffer (MB), containing 6M GTC, 10mM Tris–HCl pH 6.8, 20mM EDTA, 4% Triton X-100, 1% Sarkosyl and 1% DTT. DNA was precipitated by adding 1ml of 100% ethanol and was washed three times in wash buffer (20mM Tris-HCl pH 6.8, 150mM NaCl and 50% ethanol) and DNA was solubilized in 1ml of 8mM NaOH. A small aliquot of the recovered DNA was digested with 50mg/ml proteinase K for 3 hours at 50°C and quantified using Qubit dsDNA HS Assay Kit according to manufacturer instructions. DNA concentration was further confirmed by slot-blot where the proteinase K digested samples were diluted in TBS buffer and applied to nylon membrane (Hybond N+) followed by immunodetection with antibody against dsDNA. 10µg DNA were precipitated by addition of 1:10 volume of 3M sodium acetate sodium acetate and 2.5 volume of 200 proof ethanol. After 20 min of centrifugation at high speed, DNA was resuspended in 60µl of ddH_2O and digested with Benzonase for 30min at 37°C. At last, 4xSDS sample loading buffer was added to the digested samples followed by gel electrophoresis on 4 to 15% precast polyacrylamide gel for immunodetection for total Top1-DPCs.

DNA fiber labeling

Doxycycline induced optoSLX4 cells were sequentially labeled with two halogenated thymidine analogs, 5-Iodo-20-deoxyuridine (IdU at 25mM) and 5-Chloro-20-deoxyuridine (CldU at 50mM) for 30 min each. Then, SLX4 condensation was optogenetically induced with 3 min of light (4s) and dark (10s) cycles, every 30 min, for 2 hours. Cells were harvested and resuspended in ice-cold PBS. Two microliters of cell suspension were deposited on a microscope slide, and 7µL of spreading buffer (200mM Tris-HCl pH 7.5, 50mM EDTA, 0.5% SDS) was added on top for 3 min. DNA fibers were stretched by tilting the slide and letting the drop run down slowly. Following fixation in a 3:1 solution of off methanol: acetic acid, the DNA was denatured with 2.5N HCl and blocked with PBS/1%BSA/0.1% Tween. DNA spreads were immunostained with mouse anti-BrdU, rat anti-CldU and mouse anti-ssDNA antibodies. Corresponding secondary antibodies conjugated to Alexa Fluor dyes were used later. Images were captured using a 40x objective (NA 1.4 oil). The acquired DNA fiber images were analyzed by using ImageJ (NIH). Statistical analysis was performed with GraphPad Prism 8. Mean values were indicated by red lines. One-way ANOVA analysis was applied to compare the means of samples in a group.

Image analysis and quantification

Foci number quantification was done with ImageJ (NIH) using a manual pipeline based on segmenting nuclei and assessing foci number by the function Find Maxima.

To measure colocalization by Pearson correlation coefficient, the EzColocalization plugin was used (Stauffer et al. 2018). A threshold algorithm was used to detect nuclei then a Watershed segmentation was selected in the plugin to compute the PCC value per nucleus.

Statistical analysis and reproducibility

All statistical procedures performed are indicated in the figure legends. Each experiment was repeated independently at least three times with similar results, unless otherwise stated.

Molecular simulations

SLX4 molecules were represented as stickers-spacers polymers by means of a minimal model where only the BTB domain, the SIM domains, and the SUMOylation domains are represented explicitly with a one-bead-per-domain resolution. Consecutive domains were bound by harmonic bonds:

$$U_{b,ij} = a_{ij}\left(r - r_{0,ij}\right)^2 + b_{ij}$$

where a_{ij}, $r_{0,ij}$, and b_{ij} were parameterized to emulate the end-to-end distance distribution of the segments between the domains obtained with the Mpipi model by (*80*), which has been shown to reproduce semi-quantitatively the size of disordered proteins (see Supplemental Table 1). BTB-mediated SLX4 dimers were modeled as two monomers sharing the same BTB domain (Fig. 2**C**). SIM-SUMO interactions were modeled with an attractive potential previously introduced to simulate the condensation of associative biopolymers (*49*)**,** with the following form

$$U_{-SUMO}(r) = \frac{-1}{2} U_0 \left(1 + cos\left(\frac{\pi r}{r_0}\right)\right), r < r_c$$

where U_0 was set to 15 k_BT in order to approximately reproduce the experimental dissociation constant for SUMO/SIM complexes of 10 μM, and r_c is the cut-off distance for the interaction, set to 0.8nm. Simulations were run also with U_0 of 13 k_BT and 17 k_BT, corresponding respectively to K_D of 100 μM and 1 μM, with qualitatively similar results (Fig. S2B). All other non-bonded interactions, with the exception of those involving deSUMOylated domains, are modeled by means of the repulsive part of the Lennard-Jones potential:

$$U_{rep} = -4\varepsilon\left(\left(\frac{r_c}{r}\right)^{12} - \left(\frac{r_c}{r}\right)^{6}\right), r < r_c$$

where ε is set to 1 k_BT. The combination of these two interactions allows to impose a one-to-one valence between SIM domains and SUMO groups. All non-bonded interactions with deSUMOylated groups were ignored. Non-bonded interactions between bonded particles were evaluated, in order to take into account intramolecular formation of SUMO/SIM complexes. All simulations were run with GROMACS 2019.6 (*81*), using a Langevin dynamics integrator with a timestep of 0.01 ps and a time constant coupling of 100 ps. In one-bead-per-domain simulations, all particles had a mass of 100 Da. Bonded and non-bonded interactions were implemented as tabulated potentials. Simulations were run in cubic boxes with periodic boundary conditions in the NVT ensemble at a temperature of 300 K. Systems at different concentrations of SLX4 were obtained by changing the size of the simulation boxes, keeping constant the number of molecules, i.e. 500 in the case of monomers of SLX4 and 250 in the case of BTB-mediated SLX4 dimers, thus maintaining the same number of SIM and SUMO particles in all simulated systems. Systems at concentrations of 10 and 100 μM were simulated for 50'000'000 steps, while systems at concentrations of 1 μM were simulated for 200'000'000 steps due to longer equilibration times needed to observe the formation of condensed phases at low concentrations. The fraction of chains in the condensed phase was evaluated by considering the number of chains with at least one SUMO/SIM contact with two other chains. SUMO and SIM groups were considered in contact when their distance was below the cut-off

distance r_c. Distances between SUMO and SIM domains were evaluated by means of the gmx pairdist tool in GROMACS 2019.6 (*81*).

References:

1. V. Spegg, M. Altmeyer, Biomolecular condensates at sites of DNA damage: More than just a phase. *DNA Repair (Amst)*. **106**, 103179 (2021).

2. R. Oshidari, R. Huang, M. Medghalchi, E. Y. W. Tse, N. Ashgriz, H. O. Lee, H. Wyatt, K. Mekhail, DNA repair by Rad52 liquid droplets. *Nat Commun*. **11**, 695 (2020).

3. S. Kilic, A. Lezaja, M. Gatti, E. Bianco, J. Michelena, R. Imhof, M. Altmeyer, Phase separation of 53BP1 determines liquid-like behavior of DNA repair compartments. *The EMBO Journal*. **e101379** (2019), doi:https://doi.org/10.15252/embj.2018101379.

4. C. Frattini, A. Promonet, E. Alghoul, S. Vidal-Eychenie, M. Lamarque, M.-P. Blanchard, S. Urbach, J. Basbous, A. Constantinou, TopBP1 assembles nuclear condensates to switch on ATR signaling. *Mol Cell*. **81**, 1231-1245.e8 (2021).

5. A. S. Lyon, W. B. Peeples, M. K. Rosen, A framework for understanding the functions of biomolecular condensates across scales. *Nat Rev Mol Cell Biol*. **22**, 215–235 (2021).

6. S. F. Banani, H. O. Lee, A. A. Hyman, M. K. Rosen, Biomolecular condensates: organizers of cellular biochemistry. *Nat Rev Mol Cell Biol*. **18**, 285–298 (2017).

7. B. S. Schuster, R. M. Regy, E. M. Dolan, A. Kanchi Ranganath, N. Jovic, S. D. Khare, Z. Shi, J. Mittal, Biomolecular Condensates: Sequence Determinants of Phase Separation, Microstructural Organization, Enzymatic Activity, and Material Properties. *J Phys Chem B*. **125**, 3441–3451 (2021).

8. Y. Zhang, G. J. Narlikar, T. G. Kutateladze, Enzymatic Reactions inside Biological Condensates. *J Mol Biol*. **433**, 166624 (2021).

9. T. Mittag, R. V. Pappu, A conceptual framework for understanding phase separation and addressing open questions and challenges. *Molecular Cell*. **82**, 2201–2214 (2022).

10. R. J. Wheeler, A. A. Hyman, Controlling compartmentalization by non-membrane-bound organelles. *Philos Trans R Soc Lond B Biol Sci*. **373**, 20170193 (2018).

11. S. Alberti, A. Gladfelter, T. Mittag, Considerations and Challenges in Studying Liquid-Liquid Phase Separation and Biomolecular Condensates. *Cell*. **176**, 419–434 (2019).

12. M. Lisby, J. H. Barlow, R. C. Burgess, R. Rothstein, Choreography of the DNA damage response: spatiotemporal relationships among checkpoint and repair proteins. *Cell*. **118**, 699–713 (2004).

13. J.-M. Choi, F. Dar, R. V. Pappu, LASSI: A lattice model for simulating phase transitions of multivalent proteins. *PLoS Comput Biol*. **15**, e1007028 (2019).

14. J. R. Espinosa, J. A. Joseph, I. Sanchez-Burgos, A. Garaizar, D. Frenkel, R. Collepardo-Guevara, Liquid network connectivity regulates the stability and composition of biomolecular condensates with many components. *PNAS*. **117**, 13238–13247 (2020).

15. J. Guillén-Boixet, A. Kopach, A. S. Holehouse, S. Wittmann, M. Jahnel, R. Schlüßler, K. Kim, I. R. E. A. Trussina, J. Wang, D. Mateju, I. Poser, S. Maharana, M. Ruer-Gruß, D. Richter, X. Zhang, Y.-T. Chang, J. Guck, A. Honigmann, J. Mahamid, A. A. Hyman, R. V. Pappu, S. Alberti, T. M.

Franzmann, RNA-Induced Conformational Switching and Clustering of G3BP Drive Stress Granule Assembly by Condensation. *Cell*. **181**, 346-361.e17 (2020).

16. J. A. Riback, L. Zhu, M. C. Ferrolino, M. Tolbert, D. M. Mitrea, D. W. Sanders, M.-T. Wei, R. W. Kriwacki, C. P. Brangwynne, Composition-dependent thermodynamics of intracellular phase separation. *Nature*. **581**, 209–214 (2020).

17. D. W. Sanders, N. Kedersha, D. S. W. Lee, A. R. Strom, V. Drake, J. A. Riback, D. Bracha, J. M. Eeftens, A. Iwanicki, A. Wang, M.-T. Wei, G. Whitney, S. M. Lyons, P. Anderson, W. M. Jacobs, P. Ivanov, C. P. Brangwynne, Competing Protein-RNA Interaction Networks Control Multiphase Intracellular Organization. *Cell*. **181**, 306-324.e28 (2020).

18. P. Yang, C. Mathieu, R.-M. Kolaitis, P. Zhang, J. Messing, U. Yurtsever, Z. Yang, J. Wu, Y. Li, Q. Pan, J. Yu, E. W. Martin, T. Mittag, H. J. Kim, J. P. Taylor, G3BP1 Is a Tunable Switch that Triggers Phase Separation to Assemble Stress Granules. *Cell*. **181**, 325-345.e28 (2020).

19. J. Soding, D. Zwicker, S. Sohrabi-Jahromi, M. Boehning, J. Kirschbaum, Mechanisms for Active Regulation of Biomolecular Condensates. *Trends Cell Biol*. **30**, 4–14 (2020).

20. I. Psakhye, S. Jentsch, Protein group modification and synergy in the SUMO pathway as exemplified in DNA repair. *Cell*. **151**, 807–820 (2012).

21. C. S. Wu, J. Ouyang, E. Mori, H. D. Nguyen, A. Marechal, A. Hallet, D. J. Chen, L. Zou, SUMOylation of ATRIP potentiates DNA damage signaling by boosting multiple protein interactions in the ATR pathway. *Genes Dev*. **28**, 1472–84 (2014).

22. N. Hattersley, L. Shen, E. G. Jaffray, R. T. Hay, The SUMO protease SENP6 is a direct regulator of PML nuclear bodies. *Mol Biol Cell*. **22**, 78–90 (2011).

23. S. Müller, A. Dejean, Viral immediate-early proteins abrogate the modification by SUMO-1 of PML and Sp100 proteins, correlating with nuclear body disruption. *J Virol*. **73**, 5137–5143 (1999).

24. T. H. Shen, H.-K. Lin, P. P. Scaglioni, T. M. Yung, P. P. Pandolfi, The mechanisms of PML-nuclear body formation. *Mol Cell*. **24**, 331–339 (2006).

25. S. Weidtkamp-Peters, T. Lenser, D. Negorev, N. Gerstner, T. G. Hofmann, G. Schwanitz, C. Hoischen, G. Maul, P. Dittrich, P. Hemmerich, Dynamics of component exchange at PML nuclear bodies. *J Cell Sci*. **121**, 2731–2743 (2008).

26. Y. Kim, F. P. Lach, R. Desetty, H. Hanenberg, A. D. Auerbach, A. Smogorzewska, Mutations of the SLX4 gene in Fanconi anemia. *Nat Genet*. **43**, 142–6 (2011).

27. C. Stoepker, K. Hain, B. Schuster, Y. Hilhorst-Hofstee, M. A. Rooimans, J. Steltenpool, A. B. Oostra, K. Eirich, E. T. Korthof, A. W. Nieuwint, N. G. Jaspers, T. Bettecken, H. Joenje, D. Schindler, J. Rouse, J. P. de Winter, SLX4, a coordinator of structure-specific endonucleases, is mutated in a new Fanconi anemia subtype. *Nat Genet*. **43**, 138–41 (2011).

28. M. C. Kottemann, A. Smogorzewska, Fanconi anaemia and the repair of Watson and Crick DNA crosslinks. *Nature*. **493**, 356–63 (2013).

29. S. Minocherhomji, S. Ying, V. A. Bjerregaard, S. Bursomanno, A. Aleliunaite, W. Wu, H. W. Mankouri, H. Shen, Y. Liu, I. D. Hickson, Replication stress activates DNA repair synthesis in mitosis. *Nature*. **528**, 286–290 (2015).

30. S. L. Andersen, D. T. Bergstralh, K. P. Kohl, J. R. LaRocque, C. B. Moore, J. Sekelsky, Drosophila MUS312 and the vertebrate ortholog BTBD12 interact with DNA structure-specific endonucleases in DNA repair and recombination. *Mol Cell*. **35**, 128–35 (2009).

31. S. Fekairi, S. Scaglione, C. Chahwan, E. R. Taylor, A. Tissier, S. Coulon, M. Q. Dong, C. Ruse, J. R. Yates, P. Russell, R. P. Fuchs, C. H. McGowan, P. H. Gaillard, Human SLX4 is a Holliday junction resolvase subunit that binds multiple DNA repair/recombination endonucleases. *Cell*. **138**, 78–89 (2009).

32. I. M. Munoz, K. Hain, A. C. Declais, M. Gardiner, G. W. Toh, L. Sanchez-Pulido, J. M. Heuckmann, R. Toth, T. Macartney, B. Eppink, R. Kanaar, C. P. Ponting, D. M. Lilley, J. Rouse, Coordination of structure-specific nucleases by human SLX4/BTBD12 is required for DNA repair. *Mol Cell*. **35**, 116–27 (2009).

33. J. M. Svendsen, A. Smogorzewska, M. E. Sowa, B. C. O'Connell, S. P. Gygi, S. J. Elledge, J. W. Harper, Mammalian BTBD12/SLX4 assembles a Holliday junction resolvase and is required for DNA repair. *Cell*. **138**, 63–77 (2009).

34. H. D. M. Wyatt, S. Sarbajna, J. Matos, S. C. West, Coordinated actions of SLX1-SLX4 and MUS81-EME1 for Holliday junction resolution in human cells. *Mol Cell*. **52**, 234–247 (2013).

35. H. D. M. Wyatt, R. C. Laister, S. R. Martin, C. H. Arrowsmith, S. C. West, The SMX DNA Repair Tri-nuclease. *Mol Cell*. **65**, 848-860.e11 (2017).

36. W. S. Hoogenboom, R. A. C. M. Boonen, P. Knipscheer, The role of SLX4 and its associated nucleases in DNA interstrand crosslink repair. *Nucleic Acids Res*. **47**, 2377–2388 (2019).

37. J. Sarkar, B. Wan, J. Yin, H. Vallabhaneni, K. Horvath, T. Kulikowicz, V. A. Bohr, Y. Zhang, M. Lei, Y. Liu, SLX4 contributes to telomere preservation and regulated processing of telomeric joint molecule intermediates. *Nucleic Acids Res*. **43**, 5912–5923 (2015).

38. B. Wan, J. Yin, K. Horvath, J. Sarkar, Y. Chen, J. Wu, K. Wan, J. Lu, P. Gu, E. Y. Yu, N. F. Lue, S. Chang, Y. Liu, M. Lei, SLX4 assembles a telomere maintenance toolkit by bridging multiple endonucleases with telomeres. *Cell Rep*. **4**, 861–869 (2013).

39. J. S. J. Wilson, A. M. Tejera, D. Castor, R. Toth, M. A. Blasco, J. Rouse, Localization-dependent and -independent roles of SLX4 in regulating telomeres. *Cell Rep*. **4**, 853–860 (2013).

40. R. Elango, A. Panday, F. P. Lach, N. A. Willis, K. Nicholson, E. E. Duffey, A. Smogorzewska, R. Scully, The structure-specific endonuclease complex SLX4-XPF regulates Tus-Ter-induced homologous recombination. *Nat Struct Mol Biol*. **29**, 801–812 (2022).

41. R. Ishimoto, Y. Tsuzuki, T. Matsumura, S. Kurashige, K. Enokitani, K. Narimatsu, M. Higa, N. Sugimoto, K. Yoshida, M. Fujita, SLX4-XPF mediates DNA damage responses to replication stress induced by DNA-protein interactions. *J Cell Biol*. **220**, e202003148 (2021).

42. J. Ouyang, E. Garner, A. Hallet, H. D. Nguyen, K. A. Rickman, G. Gill, A. Smogorzewska, L. Zou, Noncovalent interactions with SUMO and ubiquitin orchestrate distinct functions of the SLX4 complex in genome maintenance. *Mol Cell*. **57**, 108–122 (2015).

43. M. Palayam, J. Ganapathy, A. M. Guercio, L. Tal, S. L. Deck, N. Shabek, Structural insights into photoactivation of plant Cryptochrome-2. *Commun Biol.* **4**, 28 (2021).

44. J. Yin, B. Wan, J. Sarkar, K. Horvath, J. Wu, Y. Chen, G. Cheng, K. Wan, P. Chin, M. Lei, Y. Liu, Dimerization of SLX4 contributes to functioning of the SLX4-nuclease complex. *Nucleic Acids Res.* **44**, 4871–4880 (2016).

45. S. F. Banani, A. M. Rice, W. B. Peeples, Y. Lin, S. Jain, R. Parker, M. K. Rosen, Compositional Control of Phase-Separated Cellular Bodies. *Cell.* **166**, 651–663 (2016).

46. K. Bhandari, M. A. Cotten, J. Kim, M. K. Rosen, J. D. Schmit, Structure-Function Properties in Disordered Condensates. *J Phys Chem B.* **125**, 467–476 (2021).

47. I. A. Hendriks, D. Lyon, C. Young, L. J. Jensen, A. C. O. Vertegaal, M. L. Nielsen, Site-specific mapping of the human SUMO proteome reveals co-modification with phosphorylation. *Nat Struct Mol Biol.* **24**, 325–336 (2017).

48. Y. Zhang, B. Xu, B. G. Weiner, Y. Meir, N. S. Wingreen, Decoding the physical principles of two-component biomolecular phase separation. *eLife.* **10**, e62403 (2021).

49. J. H. Guervilly, A. Takedachi, V. Naim, S. Scaglione, C. Chawhan, Y. Lovera, E. Despras, I. Kuraoka, P. Kannouche, F. Rosselli, P. H. L. Gaillard, The SLX4 complex is a SUMO E3 ligase that impacts on replication stress outcome and genome stability. *Mol Cell.* **57**, 123–37 (2015).

50. A. P. Jalihal, S. Pitchiaya, L. Xiao, P. Bawa, X. Jiang, K. Bedi, A. Parolia, M. Cieslik, M. Ljungman, A. M. Chinnaiyan, N. G. Walter, Multivalent Proteins Rapidly and Reversibly Phase-Separate upon Osmotic Cell Volume Change. *Mol Cell.* **79**, 978-990.e5 (2020).

51. K. Wagner, K. Kunz, T. Piller, G. Tascher, S. Hölper, P. Stehmeier, J. Keiten-Schmitz, M. Schick, U. Keller, S. Müller, The SUMO Isopeptidase SENP6 Functions as a Rheostat of Chromatin Residency in Genome Maintenance and Chromosome Dynamics. *Cell Rep.* **29**, 480-494.e5 (2019).

52. G. D. Grant, K. M. Kedziora, J. C. Limas, J. G. Cook, J. E. Purvis, Accurate delineation of cell cycle phase transitions in living cells with PIP-FUCCI. *Cell Cycle.* **17**, 2496–2516 (2018).

53. T. C. Branon, J. A. Bosch, A. D. Sanchez, N. D. Udeshi, T. Svinkina, S. A. Carr, J. L. Feldman, N. Perrimon, A. Y. Ting, Efficient proximity labeling in living cells and organisms with TurboID. *Nat Biotechnol.* **36**, 880–887 (2018).

54. E. Alghoul, J. Basbous, A. Constantinou, An optogenetic proximity labeling approach to probe the composition of inducible biomolecular condensates in cultured cells. *STAR Protoc.* **2**, 100677 (2021).

55. K. Luo, H. Zhang, L. Wang, J. Yuan, Z. Lou, Sumoylation of MDC1 is important for proper DNA damage response. *EMBO J.* **31**, 3008–3019 (2012).

56. J. R. Morris, C. Boutell, M. Keppler, R. Densham, D. Weekes, A. Alamshah, L. Butler, Y. Galanty, L. Pangon, T. Kiuchi, T. Ng, E. Solomon, The SUMO modification pathway is involved in the BRCA1 response to genotoxic stress. *Nature.* **462**, 886–890 (2009).

57. C. A. Cremona, P. Sarangi, Y. Yang, L. E. Hang, S. Rahman, X. Zhao, Extensive DNA damage-induced sumoylation contributes to replication and repair and acts in addition to the mec1 checkpoint. *Mol Cell*. **45**, 422–432 (2012).

58. S. P. Jackson, D. Durocher, Regulation of DNA damage responses by ubiquitin and SUMO. *Mol Cell*. **49**, 795–807 (2013).

59. J. Torres-Rosell, I. Sunjevaric, G. De Piccoli, M. Sacher, N. Eckert-Boulet, R. Reid, S. Jentsch, R. Rothstein, L. Aragón, M. Lisby, The Smc5-Smc6 complex and SUMO modification of Rad52 regulates recombinational repair at the ribosomal gene locus. *Nat Cell Biol*. **9**, 923–931 (2007).

60. Y. Galanty, R. Belotserkovskaya, J. Coates, S. P. Jackson, RNF4, a SUMO-targeted ubiquitin E3 ligase, promotes DNA double-strand break repair. *Genes Dev*. **26**, 1179–1195 (2012).

61. Y. Yin, A. Seifert, J. S. Chua, J.-F. Maure, F. Golebiowski, R. T. Hay, SUMO-targeted ubiquitin E3 ligase RNF4 is required for the response of human cells to DNA damage. *Genes Dev*. **26**, 1196–1208 (2012).

62. Y. Sun, L. M. Miller Jenkins, Y. P. Su, K. C. Nitiss, J. L. Nitiss, Y. Pommier, A conserved SUMO pathway repairs topoisomerase DNA-protein cross-links by engaging ubiquitin-mediated proteasomal degradation. *Sci Adv*. **6**, eaba6290 (2020).

63. J. C. Y. Liu, U. Kühbacher, N. B. Larsen, N. Borgermann, D. H. Garvanska, I. A. Hendriks, L. Ackermann, P. Haahr, I. Gallina, C. Guérillon, E. Branigan, R. T. Hay, Y. Azuma, M. L. Nielsen, J. P. Duxin, N. Mailand, Mechanism and function of DNA replication-independent DNA-protein crosslink repair via the SUMO-RNF4 pathway. *EMBO J*. **40**, e107413 (2021).

64. D. B. Krastev, S. Li, Y. Sun, A. J. Wicks, G. Hoslett, D. Weekes, L. M. Badder, E. G. Knight, R. Marlow, M. C. Pardo, L. Yu, T. T. Talele, J. Bartek, J. S. Choudhary, Y. Pommier, S. J. Pettitt, A. N. J. Tutt, K. Ramadan, C. J. Lord, The ubiquitin-dependent ATPase p97 removes cytotoxic trapped PARP1 from chromatin. *Nat Cell Biol* (2022), doi:10.1038/s41556-021-00807-6.

65. J. R. Mullen, V. Kaliraman, S. S. Ibrahim, S. J. Brill, Requirement for three novel protein complexes in the absence of the Sgs1 DNA helicase in Saccharomyces cerevisiae. *Genetics*. **157**, 103–118 (2001).

66. Y. Kim, G. S. Spitz, U. Veturi, F. P. Lach, A. D. Auerbach, A. Smogorzewska, Regulation of multiple DNA repair pathways by the Fanconi anemia protein SLX4. *Blood*. **121**, 54–63 (2013).

67. N. Serbyn, I. Bagdiul, A. Noireterre, A. H. Michel, R. T. Suhandynata, H. Zhou, B. Kornmann, F. Stutz, SUMO orchestrates multiple alternative DNA-protein crosslink repair pathways. *Cell Rep*. **37**, 110034 (2021).

68. K. Fugger, W. K. Chu, P. Haahr, A. N. Kousholt, H. Beck, M. J. Payne, K. Hanada, I. D. Hickson, C. S. Sørensen, FBH1 co-operates with MUS81 in inducing DNA double-strand breaks and cell death following replication stress. *Nat Commun*. **4**, 1423 (2013).

69. E. Malacaria, A. Franchitto, P. Pichierri, SLX4 Prevents GEN1-Dependent DSBs During DNA Replication Arrest Under Pathological Conditions in Human Cells. *Sci Rep*. **7**, 44464 (2017).

70. A. M. Carr, A. L. Paek, T. Weinert, DNA replication: failures and inverted fusions. *Semin Cell Dev Biol*. **22**, 866–874 (2011).

71. R. L. Ragland, S. Patel, R. S. Rivard, K. Smith, A. A. Peters, A.-K. Bielinsky, E. J. Brown, RNF4 and PLK1 are required for replication fork collapse in ATR-deficient cells. *Genes Dev*. **27**, 2259–2273 (2013).

72. A. Takedachi, E. Despras, S. Scaglione, R. Guérois, J. H. Guervilly, M. Blin, S. Audebert, L. Camoin, Z. Hasanova, M. Schertzer, A. Guille, D. Churikov, I. Callebaut, V. Naim, M. Chaffanet, J. P. Borg, F. Bertucci, P. Revy, D. Birnbaum, A. Londoño-Vallejo, P. L. Kannouche, P. H. L. Gaillard, SLX4 interacts with RTEL1 to prevent transcription-mediated DNA replication perturbations. *Nat Struct Mol Biol*. **27**, 438–449 (2020).

73. S. J. Young, M. Sebald, R. Shah Punatar, M. Larin, L. Masino, M. C. Rodrigo-Brenni, C.-C. Liang, S. C. West, MutSβ Stimulates Holliday Junction Resolution by the SMX Complex. *Cell Rep*. **33**, 108289 (2020).

74. M. Bienz, Head-to-Tail Polymerization in the Assembly of Biomolecular Condensates. *Cell*. **182**, 799–811 (2020).

75. W. Peeples, M. K. Rosen, Mechanistic dissection of increased enzymatic rate in a phase-separated compartment. *Nat Chem Biol*. **17**, 693–702 (2021).

76. F. B. Couch, C. E. Bansbach, R. Driscoll, J. W. Luzwick, G. G. Glick, R. Bétous, C. M. Carroll, S. Y. Jung, J. Qin, K. A. Cimprich, D. Cortez, ATR phosphorylates SMARCAL1 to prevent replication fork collapse. *Genes Dev*. **27**, 1610–1623 (2013).

77. V. Lallemand-Breitenbach, H. de Thé, PML nuclear bodies: from architecture to function. *Curr Opin Cell Biol*. **52**, 154–161 (2018).

78. U. Sahin, O. Ferhi, M. Jeanne, S. Benhenda, C. Berthier, F. Jollivet, M. Niwa-Kawakita, O. Faklaris, N. Setterblad, H. de Thé, V. Lallemand-Breitenbach, Oxidative stress–induced assembly of PML nuclear bodies controls sumoylation of partner proteins. *Journal of Cell Biology*. **204**, 931–945 (2014).

79. J. A. Joseph, A. Reinhardt, A. Aguirre, P. Y. Chew, K. O. Russell, J. R. Espinosa, A. Garaizar, R. Collepardo-Guevara, Physics-driven coarse-grained model for biomolecular phase separation with near-quantitative accuracy. *Nat Comput Sci*. **1**, 732–743 (2021).

80. M. J. Abraham, T. Murtola, R. Schulz, S. Páll, J. C. Smith, B. Hess, E. Lindahl, GROMACS: High performance molecular simulations through multi-level parallelism from laptops to supercomputers. *SoftwareX*. **1–2**, 19–25 (2015).

Figure legends

Figure 1. SLX4 forms light-inducible dynamic compartments

A. Schematic representation of the optognetic activation of SLX4 condensates.
B. Optogenetic activation of optoSLX4 after inducing its expression by doxycycline. Light on consists of 4 min cycles of 4 seconds light (488 nm) and 10 seconds dark. Representative images are shown with a scale bar of 10µm. Violin plot represents distribution of number of foci per cell. Data are plotted as medians with quartiles (n>100 cells per condition collected from 2 independent experiments). The statistical significance between samples is represented by asterisks.
C. Time-lapse microscopy showing in real time the induction of optoSLX4 compartments along with a fusion event.
D. Representative images showing the dissolution of optoSLX4 compartments, 30 min after light activation. Scale bar 10µm. Activated cells were left in the dark for the corresponding duration. The number of foci per nucleus is quantified in the histogram. Data are plotted as medians with s.d. (n>100 cells per condition collected from 3 independent experiments).
E. Example images of optoSLX4 cells expressing an increasing level of the construct (proportional to the concentration of doxycycline added to the medium). Spontaneous nuclear compartments are counted. No light induction was made. Scale bar 10µm. The relative amount of the optoSLX4 construct is shown in the blot. Data are plotted as medians with s.d. (n>100 cells per condition collected from 3 independent experiments).

Figure 2. Structural determinants of SLX4 condensation

A. Disorder score of human SLX4 by PONDR VSL2 prediction output (upper panel). Schematic diagram of the protein constructs and truncations used to investigate the domains required for SLX4 compartmentalization (lower panel). All constructs are fused to a Cry2-mCherry module at their N-terminus.
B. Representative images showing the stable cell lines expressing the different constructs before and after light induction. The quantification of the number of foci per nucleus is shown in the corresponding violin plots. Data are plotted as medians with quartiles (n>300 cells per condition collected from 2 independent experiments).
C. Schematic representation of the molecular models of SLX4 monomer (top) and BTB-mediated dimer (bottom). Green particles are BTB domains, red particles are SIM domains, blue and white particles are SUMOylation sites.
D. Representative snapshot of condensate formation from a MD simulation of BTB-mediated dimers of SLX4 with three SUMOylated sites per monomer.
E. Fraction of chains in the condensed phase as a function of the total concentration and the number of SUMOylated sites per monomer in simulations of SLX4 monomers, where the Kd for SUMO-SIM interaction is set to 10 µM.
F. Fraction of chains in the condensed phase as a function of the total concentration and the number of SUMOylated sites per monomer in simulations of BTB-mediated SLX4 dimers, where the Kd for SUMO-SIM interaction is set to 10 µM.

Figure 3. The dimerization domain along with the SUMO-SIM interactions drive the assembly of SLX4 compartments

A. OptoSLX4 wild type, F708R and SIM*1,2,3 expressing cells prior and after induction with blue light. Scale bar 10µm. The expression level of the different constructs is depicted in the corresponding blot (upper panel).

B. Quantification of (C). Data are plotted as medians with quartiles (n>100 cells per condition collected from 3 independent experiments).

C. Representative images of optoSLX4 cells treated with ML-792 (2µM), TAK-243 (2µM) and MG-132 (10µM) for 4 hours prior to light induction and fixation for microscopy analysis. Scale bar 10µm. The quantification of SLX4 foci is shown in the corresponding violin plots of the lower panel. Data are plotted as medians with quartiles (n>100 cells per condition collected from 2 independent experiments).
D. FA patient derived RA3331 fibroblast with corrected SLX4 full length were treated with ML-792 (2µM), TAK-243 (2µM) and MG-132 (10µM) for 4 hours. CPT was added to the media in the last hour at a final concentration of 1 µM. Cells were then fixed and stained for endogenous SLX4 expression. The corresponding histogram shows the quantification of foci number per nucleus. Data are plotted as means with s.d. (n>200 cells per condition).
E. optoSLX4 cells were transfected with the indicated siRNA and induced or not with light. The foci were counted and plotted as medians with quartiles (n>200 cells per condition collected from two independent experiments).
F. Violin plots showing the quantification of optoSLX4 foci number per nucleus of GFP-SENP6-WT/C1030A transfected and untransfected cells. Data are plotted as medians with quartiles (n>100 cells per condition collected from 2 independent experiments).

Figure 4. SLX4 compartments assemble the SUMO/ubiquitin machinery

A. Quantitative analysis of the proximal and interacting proteins of SLX4 by TurboID proximity biotinylation-coupled mass spectrometry. The relative abundance of ranked proteins were estimated by the iBAQ method. Data from 7 biological replicates is shown. SUMOylation and ubiquitylation machineries are shown in red and blue respectively.
B. Schematic of the optoSLX4 module with the TurboID (upper panel). Overall scheme of the TurboID-optogenetic coupled method (lower panel).
C. Streptavidin pull-down of proteins, biotinylated by TurboID-optoSLX4 wild type were probed by immunoblotting for SLX4 and the SUMOylation machinery.
D. Representative Immunostainings showing the colocalisation of endogenous SUMO1 and SUMO2/3 with optoSLX4 compartments (upper panels). Cells transfected with GFP tagged SUMO1, SUMO2/3, UBC9 and PIAS4 showing enrichment of the SUMOylation machinery in the optoSLX4 foci (lower panels). Scale bar 10µm.

Figure 5. SLX4 compartments induce the modification of client proteins with SUMO and ubiquitin

A. Experimental strategy of the His-pulldown to enrich SUMO/Ub modified proteins upon SLX4 compartimentalisation.
B. optoSLX4 cells previously transfected with cDNA coding for His-SUMO2/3 were induced with light for the designated time in the presence or absence of doxycycline. The cells were later lysed and processed for metal affinity purification of SUMOylated proteins.
C. Cells expressing wild type, F708R and SIM*1,2,3 optoSLX4 were induced with light for 15 min prior to lysis and His-SUMO2/3 pulldown.
D. His-SUMO2/3 pulldown showing the condensation induced modification of SLX4 client proteins.
E. optoSLX4 cells were transfected with GFP-RNF4-WT or GFP-RNF4-C159A. Cells expressing the wild type form were then treated with 10µM MG-132 for 4hrs. Violin plots representing the number of optoSLX4 foci in transfected versus untransfected cells, prior or after light induction. Data are plotted as medians with quartiles (n>100 cells per condition collected from 3 independent experiments).
F. Representative images of optoSLX4 cells transfected with the indicated siRNA and induced or not with light. Scale bar 10µm. The corresponding blot showing the level of depletion of RNF4 (lower left panel). Violin plots quantifying the number of SLX4 foci per cell after the knockdown of RNF4 (lower

right panel). Data are plotted as medians with quartiles (n>100 cells per condition collected from 2 independent experiments).

G. His-pulldown of optoSLX4 cells transfected with His-Ub construct and induced with light for the corresponding time.
H. The modification of SLX4 compartment's client proteins with ubiquitin after the induction of SLX4 foci with light for 15 min.
I. His-Ub pulldown of optoSLX4 cells, previously transfected with the corresponding siRNA, prior or after light induction.

Figure 6. SLX4 compartments enhance the modification and the removal of Top1 cleavage complexes.

A. Upper panel: optoSLX4 cells were transfected with His-SUMO2/3 and activated by light prior to a denaturing His-pulldown and blotting with Top1 antibody.
Middle panel: optoSLX4 cells were transfected with His-Ub and activated by light prior to a denaturing His-pulldown and blotting with Top1 antibody.
Bottom panel: optoSLX4 cells were transfected with either siControl or siRNF4. The next day, these cells were transfected with His-Ub and activated by light prior to a denaturing His-pulldown and blotting with Top1 antibody.
B. Upper panel: Scheme illustrating the experimental set up of the DUST assay to monitor Total Top1-DPCs. optoSLX4 cells were exposed (2,3) or not (1), to 1µM CPT for 15 min. After 5 min of CPT treatment, cells were exposed to an array of blue-light during 1 min of light-dark cycles (4 sec light followed by 10 sec dark) (3). Bottom panel: optoSLX4 cells were subjected to treatment as indicated and cells were collected for DUST assay to detect total Top1-DPCs.
C. Fibroblasts with truncated SLX4 from FA patient RA3331 (FA-P + control) along with the cells with the corrected SLX4 full length version (FA-P + WT SLX4) were treated with 1µM CPT for 30 min prior to fixation. Topoisomerase I cleavage complexes (TOP1cc) were detected by immunofluorescence. The quantification of Top1cc intensity per nucleus is depicted in the violin plots. Data are plotted as medians with quartiles (n>200 cells per condition collected from 3 independent experiments).
D. Representative images showing the level of TOP1cc in treated versus untreated FA-P cells. Scale bar 20µm.
E. TOP1cc intensity per nucleus in CPT treated optoSLX4 cells induced or not with doxycycline to induce SLX4 overexpression. Data are plotted as medians with quartiles (n>200 cells per condition collected from 2 independent experiments).
F. Representative images showing the level of TOP1cc in doxycycline induced versus un-induced optoSLX4 cells. Scale bar 10µm.

Figure 7. SLX4 assembly promotes DNA end resection.

A. Schematic diagram of the DNA fiber labelling coupled optogenetic procedure.
B. Nascent DNA degradation analysis in optoSLX4 cells expressing the wild type and the condensation mutants F708R and SIM*1,2,3 before (off) or after (on) light activation. Data are plotted as medians (n>100 cells per condition collected from 3 independent experiments).
C. Resection of nascent DNA in optoSLX4-WT cells pre-treated with 2µM SUMOi ML-792. Data are plotted as medians (n>100 cells per condition collected from 2 independent experiments).
D. Same as in (C) but cells were pre-transfected with non-targeting RNA or siRNF4. Data are plotted as medians (n>100 cells per condition collected from 2 independent experiments).
E. Same as in (C) but cells were treated with 100µM Mirin (Sigma) just before the first light cycle. Data are plotted as medians (n>100 cells per condition collected from 2 independent experiments).

F. DNA resection analysis of optoSLX4-WT and a mutant that doesn't interact with the structure specific nucleases before (off) or after (on) light activation. Data are plotted as medians (n>100 cells per condition collected from 2 independent experiments).
G. Rad51 foci accumulation after 1 cycle of light induction in cells expressing or not optoSLX4-WT. Scale bar 10µm.
H. Quantification of RAD51 foci represented in (G). Data are plotted as medians (n>100 cells per condition collected from 2 independent experiments).
I. Model for the mechanism and functions of SLX4 condensates. Created with BioRender.com. SLX4 forms a reversible protein network held by BTB-BTB and SUMO-SIM interactions. This network functions as compartment to enhance selectively the modification of substrate proteins by SUMO and ubiquitin. SLX4 condensation ensures the extraction of TOP1-DPCs from chromatin and the collapse of DNA replication forks.

Supplementary Material

Tables S1

Figs. S1 to S5

Key Resources Table

Movies S1 to S3

Spreadsheet (SLX4 proximity labelling MS data)

Supplemental Table 1

Parameters for the bonded interactions between the explicit domains in the minimal model of SLX4. The first column reports the residue numbers of the SLX4 sequence of the first and last amino acids of the protein segment modeled with an harmonic bond. Note that residues between 684 and 788 correspond to the sequence of the BTB domain.

SLX4 residues	**$x_{0,ij}$ [nm]**	**a_{ij} [kJ/mol/nm^2]**	**b_{ij} [kJ/mol]**
291-684	11.5475	0.0754653	9.82136
788-902	7.76986	0.158887	9.12396
902-1151	11.2579	0.0604855	10.5146
1151-1169	2.43396	2.7647	5.0439
1169-1179	1.55051	11.3416	2.78733
1179-1194	2.10861	4.21843	4.45981
1194-1392	9.35967	0.0779045	10.0876
1392-1575	9.26161	0.0886052	10.0053
1575-1588	1.95533	5.71225	3.86846

1588-1657	5.3133	0.316272	8.21493

Supplementary Figure Legends

Figure S1

A. The relative expression level of mCherry-SLX4 in a stable inducible cell line. An increasing concentration of doxycycline is used. Tubulin is used as a loading control.
B. Representative images of mCherry-SLX4 spontaneous foci.
C. Violin plots representing the number of mCherry-SLX4 foci per nucleus. Data are plotted as medians with quartiles (n>100 cells per condition collected from 2 independent experiments).

Figure S2

A. Blot showing the level of expression of the different optoSLX4 truncations from the structure function analysis.
B. Fraction of chains in the condensed phase as a function of the total concentration and the number of SUMOylated sites per monomer in simulations of SLX4 monomers or dimers using Kd values for SUMO-SIM interactions of 1 μM or 100 μM, as indicated.
C. optoSLX4 wild type, F708R, SIM*1,2,3 were incubated for 10 min in a media containing 300 mM NaCl, sucrose, or sorbitol. Cells were then fixed, counterstained, and imaged. The experiment was conducted in the dark without light induction. The scale bar for the representative images is 10μm.
D. Quantification of (C). The corresponding histogram shows the quantification of foci number per nucleus. Data are plotted as means with s.d. (n>100 cells per condition collected from 2 independent experiments).
E. Blot showing the effect of SUMO, ubiquitin and proteasome inhibitors on optoSLX4 stability. Cells were treated with ML-792 (2μM), TAK-243 (2μM) and MG-132 (10μM) for 4 hours prior to cell lysis.
F. Blot showing the level of depletion of SENP6, 48hrs post transfection with 20nM of the corresponding siRNA.
G. Representative images showing optoSLX4 cells transfected with the indicated siRNA and induced or not with light. Scale bar 10μm.
H. Representative images showing optoSLX4 cells transfected with GFP-SENP6-WT and GFP-SENP6-C1030A before the expression and light induction of optoSLX4 compartments. Scale bar 10μm.

Figure S3

A. The sequence and position of the SLX4 nucleo-localization signal (upper panel). Representative images of optoSLX4-ΔNLS expressing cells before and after light induction. Scale bar 10μm.
B. Chromatin fractionation of optoSLX4 wild-type cells. Chromatin enrichment of the construct was checked by western blot analysis for the soluble and insoluble fractions. Tubulin and histone H3 were used as loading controls for the soluble and chromatin fractions respectively.
C. Chromatin fractionation of optoSLX4 mutants, and wild type cells treated for 4 hours with 2μM ML-792. Tubulin and histone H3 were used as loading controls for the soluble and chromatin fractions respectively.
D. Representative immunofluorescence images demonstrating the colocalisation of optoSLX4 with proteins of the DNA damage response, telomeric factors and PML after light induction. Scale bar 10μm. Line scans are depicted in the right panel.
E. Co-localization in (D) is quantified using Pearson's correlation coefficient. Medians are shown in red.
F. Representative fluorescence images showing the distribution of SLX4 spontaneous foci in different phases of the cell cycle using the FUCCI cell cycle reporter. Cells expressing Cry2-SLX4-HALO were transfected with cDNA expressing the FUCCI reporter. The expression of SLX4 was induced by

doxycycline overnight. The next day, SLX4 was labeled with JF-646. Cells were fixed and imaged. Scale bar 10µm. The violin plots in the right panel show the quantification of optoSLX4 foci.

Figure S4

A. Schematic diagram for the ex vivo/in vitro SUMOylation assay.
B. YFP-SLX4 complexes were immunoprecipitated from stable inducible HeLa YFP-SLX4 cells and incubated with recombinant E1, E2, SUMO2 ± ATP.
C. Representative images showing optoSLX4 cells transfected with GFP-RNF4-WT or GFP-RNF4-C159A. Cells expressing the wild type form were then treated with 10µM MG-132 for 4hrs. Scale bar 10µm.
D. Streptavidin pull-down of proteins, biotinylated by TurboID-optoSLX4 wild type were probed for SLX4 and ubiquitin.
E. Representative Immunostainings showing the colocalisation of endogenous mono- and polyubiquitinylated conjugates with optoSLX4 compartments. Scale bar 10µm.

Figure S5

A. Streptavidin pull-down of proteins, biotinylated by TurboID-optoSLX4 wild type were probed for SLX4 and the structure specific nucleases.
B. Cells transfected with constructs expressing GFP tagged MUS81 and SLX1 showing colocalisation and enrichment of these nucleases in SLX4 compartments. Scale bar 10µm.
C. Representative Immunostainings showing the colocalisation of endogenous XPF with optoSLX4 compartments. Scale bar 10µm.
D. Co-localization with light activated optoSLX4 compartments in (B-C) is quantified using Pearson's correlation coefficient. Medians are shown in red. n=50 cells per condition.
E. optoSLX4 wild type and SMX* expressing cells prior and after induction with blue light. Scale bar 10µm.
F. Quantification of condensates in (E). n>100 cells per condition collected from 2 independent experiments.
G. Schematic diagram of the Mirin treatment to assess its effect on SLX4 condensation.
H. Representative images of optoSLX4 cells treated with Mirin as indicates and induced or not with light. Scale bar 10µm.
I. Violin plots depicting the quantification of (H). Data are plotted as medians (n>100 cells per condition).

KEY RESOURCES TABLE

REAGENT or RESOURCE	SOURCE	IDENTIFIER
Antibodies		
Chk1	Santa Cruz Biotechnology	Cat# sc-8408; RRID:AB_627257
pChk1 (Ser345)	Cell Signaling Technology	Cat# 2348; RRID:AB_331212
TopBP1	Bethyl	Cat# A300-111A; RRID:AB_2272050
Alexa Fluor 546 goat anti-mouse IgG	Molecular Probes	Cat# A-11030; RRID:AB_144695
Alexa Fluor 546 goat anti-rabbit IgG	Molecular Probes	Cat# A-11010; RRID:AB_2534077
Alexa Fluor 488 goat anti-mouse IgG2b	Molecular Probes	Cat# A-21141; RRID:AB_141626
Alexa Fluor 488 goat anti-rabbit IgG	Molecular Probes	Cat# A-21141; RRID:AB_141626
Anti-rabbit IgG, HRP linked Antibody	Cell Signaling Technology	Cat# 7074; RRID:AB_2099233

BRCA1(C-20)	Santa Cruz Biotechnology	Cat# sc-642; RRID:AB_630944
SLX4/BTB12	Bethyl	Cat# A302-270A; RRID:AB_1850156
MDC1	Abcam	Cat# ab11169; RRID:AB_297807
PIAS4(D2F12)	Cell Signaling Technology	Cat# 4392; RRID:AB_10547884
RNF4	Novus	Cat# H00006047-A01; RRID:AB_547785
MRE11	Thermo Fisher Scientific	Cat# PA520870; RRID:AB_11151983
SENP6	Sigma-Aldrich	Cat# WH0026054M1; RRID:AB_1843525
XPF	Thermo Fisher Scientific	Cat# MA5-12054; RRID:AB_10981652
HaloTag	Promega	Cat# G9211; RRID:AB_2688011
Phospho-Histone H2A.X (Ser139)	Millipore	Cat# 05-636; RRID:AB_309864
MUS81	Abcam	Cat# ab14387; RRID:AB_301167
TRF2	Abcam	Cat# ab108997; RRID:AB_10866674
ERCC1	Abcam	Cat# ab129267; RRID:AB_11157618
Histone H3	Abcam	Cat# ab1791; RRID:AB_302613
Eme1 (MTA31 7h2/1)	Santa Cruz Biotechnology	Cat# sc-53275; RRID:AB_2278026
RANBP2	Abcam	Cat# ab64276; RRID:AB_1142517
UBC9 (C-12)	Santa Cruz Biotechnology	Cat# sc-271057; RRID:AB_10610674
SUMO-1	Cell Signaling Technology	Cat# 4930; RRID:AB_10698887
SUMO-2/3	Cell Signaling Technology	Cat# 4971; RRID:AB_2198425
Anti-Mouse-IgG - Atto 647N	Sigma-Aldrich	Cat# 50185; RRID:AB_1137661
Anti-Rabbit-IgG - Atto 647N	Sigma-Aldrich	Cat# 40839; RRID:AB_1137669
mCherry	Elabscience	Cat# E-AB-20087
Tubulin (B-5-1-2)	Sigma-Aldrich	Cat# T5168; RRID:AB_477579
GFP	Abcam	Cat# ab290; RRID:AB_303395
BrdU	BD Biosciences	Cat# 347580; RRID:AB_10015219
Topoisomerasel-DNA Covalent Complexe	Millipore	Cat# MABE1084; RRID:AB_2756354
Mono- and polyubiquitinylated conjugates, mAb (FK2)	Enzo Life Sciences	Cat# BML-PW8810; RRID:AB_10541840
Bacterial and Virus Strains		
5-alpha Competent *E. coli* (High Efficiency	NEB	Cat# C2987
Chemicals, Peptides, and Recombinant Proteins		
Biotin	Sigma-Aldrich	Cat# B4501; CAS: 58-85-5
Doxycycline	Clontech	Cat# 631311; CAS: 10592-13-9
Blasticidin	InvivoGen	Cat# ant-bl
Hygromycin	Sigma-Aldrich	Cat# H3274; CAS: 31282-04-9
Zeocin	ThermoFisher Scientific	Cat# R25001
Penicillin streptomycin	Sigma-Aldrich	Cat# P0781; ID 329820056
Ampicilin	Sigma-Aldrich	Cat# A9518; CAS: 69-52-3

cOmplete, EDTA free	Roche	Cat# 4693159001
Halt phosphatase inhibitor cocktail	ThermoFisher Scientific	Cat# 78427
Benzonase Nuclease	Sigma-Aldrich	Cat# E1014; CAS: 9025-65-4
Phusion High-Fidelity DNA polymerase	New England Biolabs	Cat# M0530S
Ethidium bromide solution	Sigma-Aldrich	Cat# E1510; CAS: 1239-45-8
Streptavidin-Agarose	Sigma-Aldrich	Cat# S1638; MDL: MCFD00082035
Dulbecco's Modified Eagle's Medium - high glucose	Sigma-Aldrich	Cat# D5796
BioWest - Fetal Bovine Serum	Eurobio Scientific	Cat# S1810
Glycerol ≥99.5%	VWR Chemicals	Cat# 24388.295; CAS: 56-81-5
Bromophenol Blue	Ethylenediaminetetraacetic acid	Cat# B0126; CAS: 115-39-9
Ethylenediaminetetraacetic acid	Ethylenediaminetetraacetic acid	Cat# EDS; CAS: 60-00-4
HEPES	Sigma-Aldrich	Cat# H3375; CAS: 7365-45-9
Sodium Chloride	VWR Chemicals	Cat# 27810-295; CAS: 7647-14-5
Ethylene glycol-bis(2-aminoethylether)-*N,N,N′,N′*-tetraacetic acid	Sigma-Aldrich	Cat# E4378; CAS: 67-42-5
Sodium deoxycholate ≥97%	Sigma-Aldrich	Cat# D6750; CAS: 302-95-4
D-Sorbitol	Sigma-Aldrich	Cat# S1876
Sucrose	Sigma-Aldrich	Cat# S9378
Triton X-100	Sigma-Aldrich	Cat# T8787; CAS: 9002-93-1
Tergitol Solution type NP-40	Sigma-Aldrich	Cat# NP40S; MDL: MFCD01779855
Sodium dodecyl sulfate 20%	BIOSOLVE	Cat# 198123; CAS:151-21-3
Tris base	Euromedex	Cat# 200923-A; CAS: 77-86-1
Dulbecco's Phosphate Buffered Saline	Sigma-Aldrich	Cat# D8537; MDL: MFCD00131855
Opti-MEM I	ThermoFisher Scientific	Cat# 31985062
Water	Sigma-Aldrich	Cat# W3500; CAS: 7732-18-5
LiCl	Sigma-Aldrich	Cat# L9650; CAS: 7447-41-8
N ethylmaleimide	Sigma-Aldrich	Cat# E3876; CAS: 128-53-0

ML792	Euromedex	Cat# SE-S8697; CAS: 1644342-14-2
Tak-243 (MNL7243)	Euromedex	Cat# SE-s8341; CAS: 1450833-55-2
Guanidine hydrochloride	Sigma-Aldrich	Cat# G3272; CAS: 50-01-1
Bovine Serum Albumin (BSA), Fraction V	Euromedex	Cat# 04-100-812-C CAS: 90604-29-8 9048-46-8
MG-132	Euromedex	Cat# SE-S2619; CAS: 1211877-36-9
Mirin	Sigma-Aldrich	Cat# M9948 ; CAS: 299953-00-7
2-Mercaptoethanol	Sigma-Aldrich	Cat# M3148 ; CAS: 60-24-2
5-Iodo-2′-deoxyuridine	Sigma-Aldrich	Cat# I7125; CAS: 54-42-2
5-Chloro-2′-deoxyuridine	Sigma-Aldrich	Cat# C6891; CAS: 50-90-8
Janelia fluor 646 halo tag	Promega	Cat# GA1121
Janelia fluor 549 halo tag	Promega	Cat# GA1110
DMSO	Sigma-Aldrich	Cat# 276855; CAS: 67-68-5
Imidazole	Sigma-Aldrich	Cat# I5513; CAS: 288-32-4
Formaldehyde 32% Sol	Euromedex	Cat# EM-15714
Sodium phosphate monobasic	Sigma-Aldrich	Cat# S0751; CAS: 7558-80-7
Sodium phosphate dibasic	Sigma-Aldrich	Cat# S0876; CAS: 7558-79-4
TWEEN® 20	Sigma-Aldrich	Cat# P9416; CAS: 9005-64-5
Hoechst 33342	Invitrogen	Cat# H1399
5-Ethynyl-2′-deoxyuridine	Santa Cruz Biotechnology	Cat# sc-284628; CAS: 61135-33-9
(*S*)-(+)-Camptothecin	Sigma-Aldrich	Cat# C9911; CAS: 7689-03-4
Hydroxyurea	Sigma-Aldrich	Cat# H8627; CAS: 127-07-1
Mitomycine C	Roche	Cat# 10107409001; CAS: 50-07-7
Urea	Sigma-Aldrich	Cat# U5378 ; CAS: 57-13-6
SPY595-DNA	Spirochrome	Cat# SC501

SPY595-DNA	Spirochrome	Cat# SC301
Critical Commercial Assays		
Clarity western ECL substrate	Bio-Rad	Cat# 170-5061
Clarity max western ECL substrate	Bio-Rad	Cat# 1705062
Criterion TGX stain free gel 7,5%	Bio-Rad	Cat# 5678024
Criterion TGX stain free gel 4-15%	Bio-Rad	Cat# 5678084
Criterion TGX stain free gel 10%	Bio-Rad	Cat# 5671034
Mini-PROTEAN TGX Stain Free Gels, 7.5%	Bio-Rad	Cat# 4568023
Mini-PROTEAN TGX Stain Free Gels, 4-15%	Bio-Rad	Cat# 4568083
Mini-PROTEAN TGX Stain Free Gels, 10%	Bio-Rad	Cat# 4568033
Trans-Blot Turbo Transfer Pack 0,2µm Nitrocellulose Midi, 10 pack	Bio-Rad	Cat# 1704159
Trans-Blot Turbo Transfer Pack 0,2µm Nitrocellulose Mini, 10 pack	Bio-Rad	Cat# 1704158
Color Prestained Protein Standard, Broad Range	BioLAbs	Cat# P7712S
Lipofectamine 2000	ThermoFisher Scientific	Cat# 11668-019
Quick Start™ Bradford 1x Dye Reagent	Bio-Rad	Cat# 500-0205
Amersham Hyperfilm ECL (8 × 10")	Dominique Dutscher	Cat# 28906839
Quick change multi site directed	Agilent technologies	Cat# 200515-5
Infusion Kit HD cloning 50Rxns	Takara Bio	Cat# 639649
Qubit 1X dsDNA HS Assay Kit	Invitrogen	Cat# Q33231
Prolong gold antifade	ThermoFisher Scientific	Cat# P10144
TALON® Metal Affinity Resin	Takara	Cat# 635501
INTERFERin	Polyplus	Cat# 409-01
Experimental Models: Cell Lines		
Flp-In™ T-REx™ 293	Invitrogen	Cat# R78007; RRID:CVCL_U427
Oligonucleotides		
siGENOME Non-Targeting siRNA Control Pools	Dharmacon_Horizon Discovery	Cat# ID:D-001206-13-20
siGENOME Human SLX4 siRNA	Dharmacon_Horizon Discovery	Cat# ID:M-014895-01-0020
siGENOME Human RNF4 siRNA	Dharmacon_Horizon Discovery	Cat# ID:M-006557-03-0020
siGENOME Human UBE2I siRNA	Dharmacon_Horizon Discovery	Cat# ID:M-004910-00-0020
	Dharmacon_Horizon	Cat# ID:M-006044-01-0020

siGENOME Human SENP6 siRNA	Discovery	
Recombinant DNA		
pCDNA5_FRT_TO_TurboID-mCherry-Cry2	Addgene	Cat# 166504; http://n2t.net/addgene:166504 ; RRID:Addgene_166504
pOG44 Flp-Recombinase Expression Vector	ThermoFisher Scientific	Cat# V600520
pLenti-CMV-Blast-PIP-FUCCI	Addgene	Cat# 138715; http://n2t.net/addgene:138715 ; RRID:Addgene_138715
pCRISPaint-HaloTag-PuroR	Addgene	Cat# 80960; http://n2t.net/addgene:80960 ; RRID:Addgene_80960
Software and Algorithms		
OMERO	OME Remote Objects software	https://www.openmicroscopy.org/
Cell Profiler 2.2.0	Cell image analysis software	https://cellprofiler.org/
Image Lab™ Software (Version 5.2.1)	Bio-Rad	http://www.bio-rad.com/fr-fr/product/image-lab-software?ID=KRE6P5E8Z
Biorender Software	Science Suite Inc.	RRID:SCR_018361
Prism 8 (Version 8.4.2)	Graphpad Software	https://www.graphpad.com/scientific-software/prism/
FIJI	Open source	https://imagej.net/Fiji
Other		
CO2 Incubator C150	Binder	Cat# 9040-0078
Sonicator, VibraCell- 72405	BioBlock scientific	N/A
KNF LABOPORT Mini Diaphragm Vacuum Pump N 811 in Pumps, Compressors	Dominique Dutscher	Cat# KNF_28002
Centrifuge Hettich Mikro 200	Grosseron	N/A
Mini-PROTEAN Tetra Vertical Electrophoresis Cell	Bio-Rad	Cat# 1658004
PowerPac™ HC High-Current Power Supply	Bio-Rad	Cat# 1645052
Trans-Blot Turbo Transfer System	Bio-Rad	Cat# 1704150

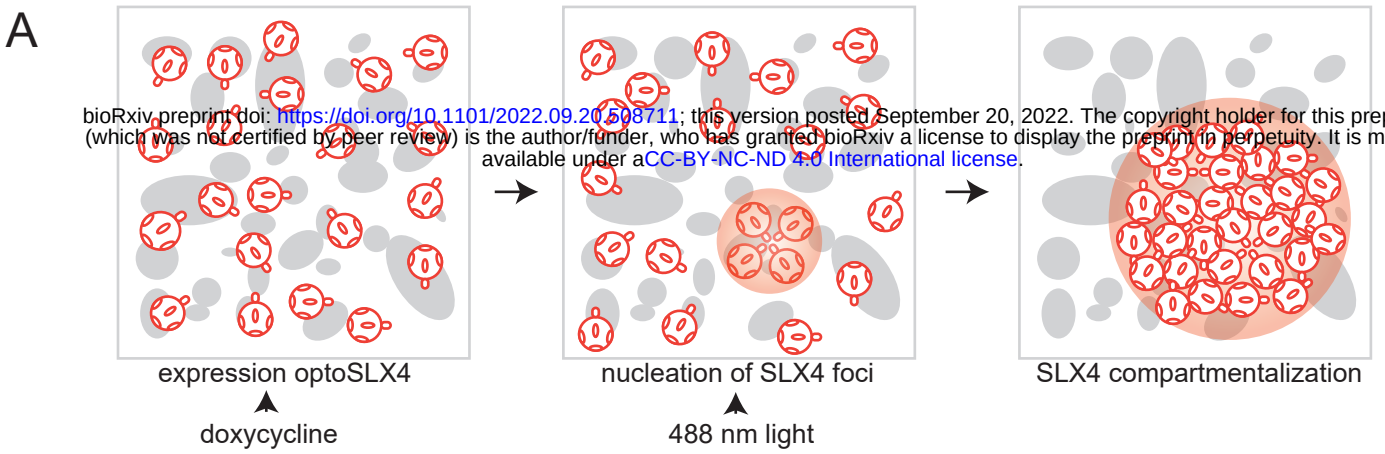

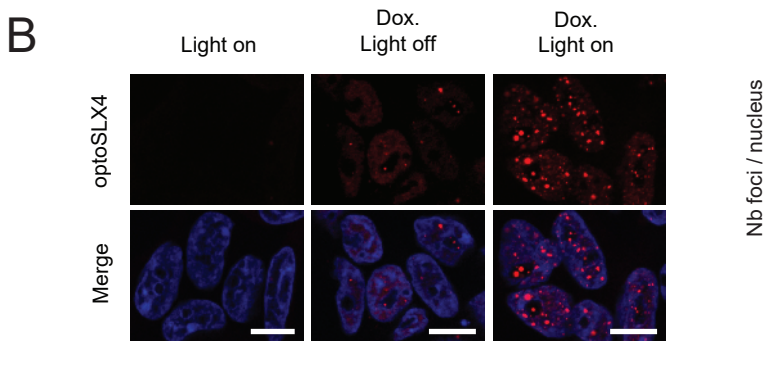

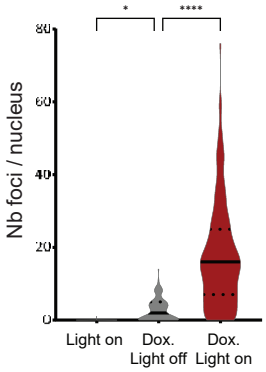

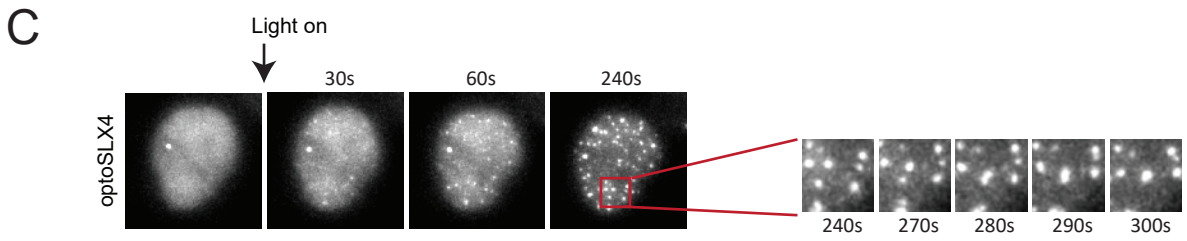

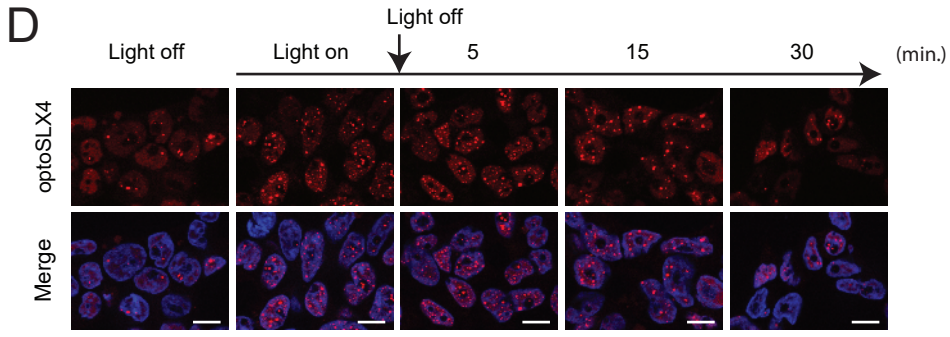

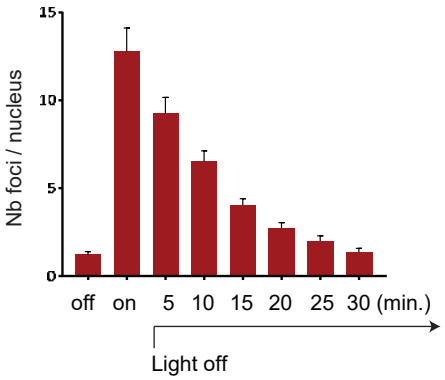

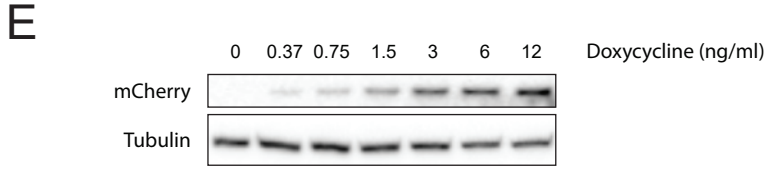

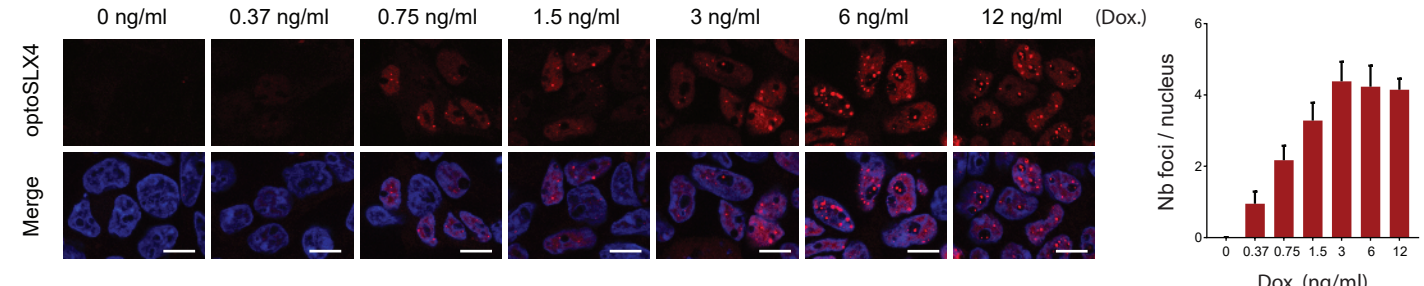

Figure 1

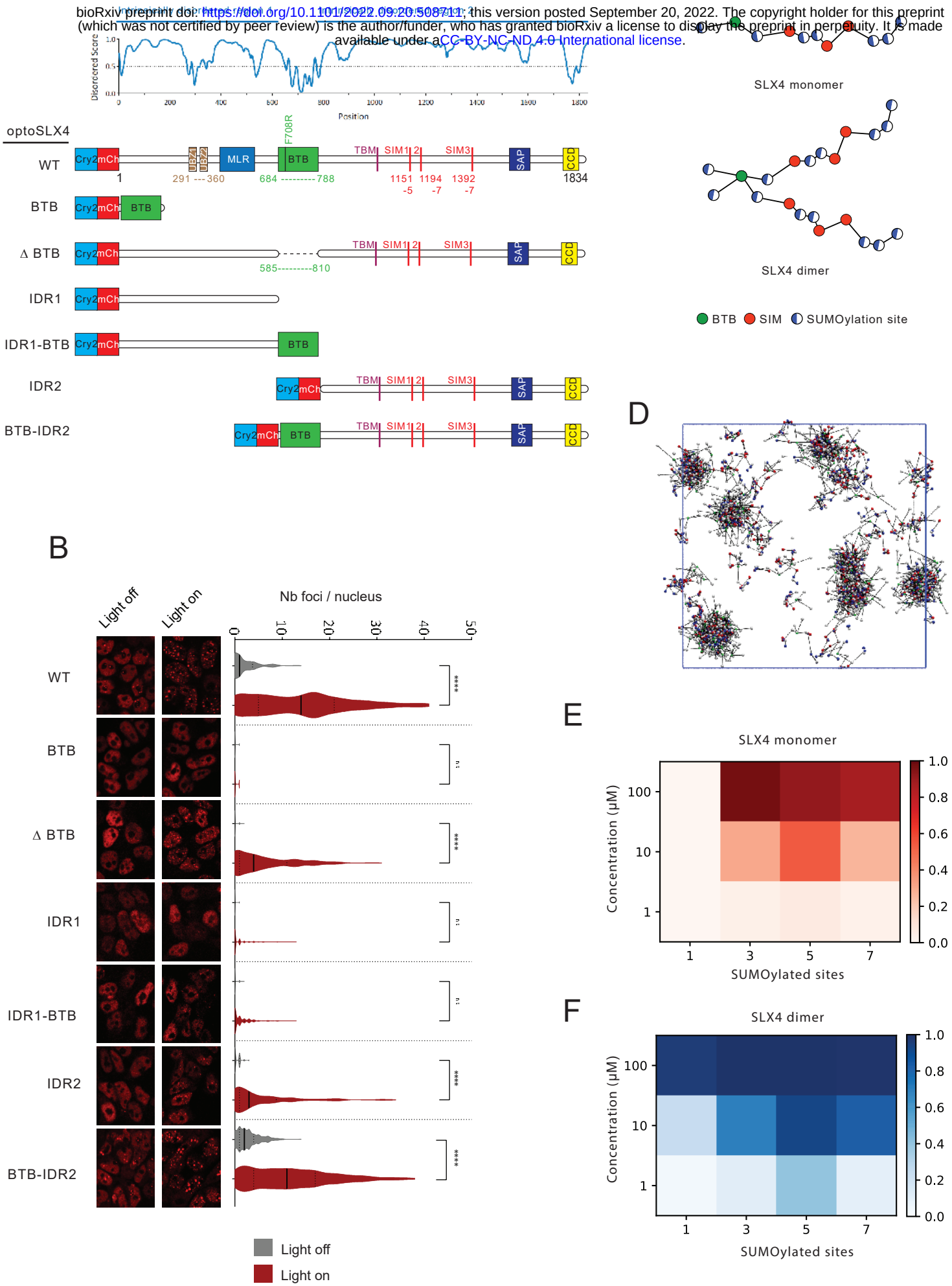

Figure 2

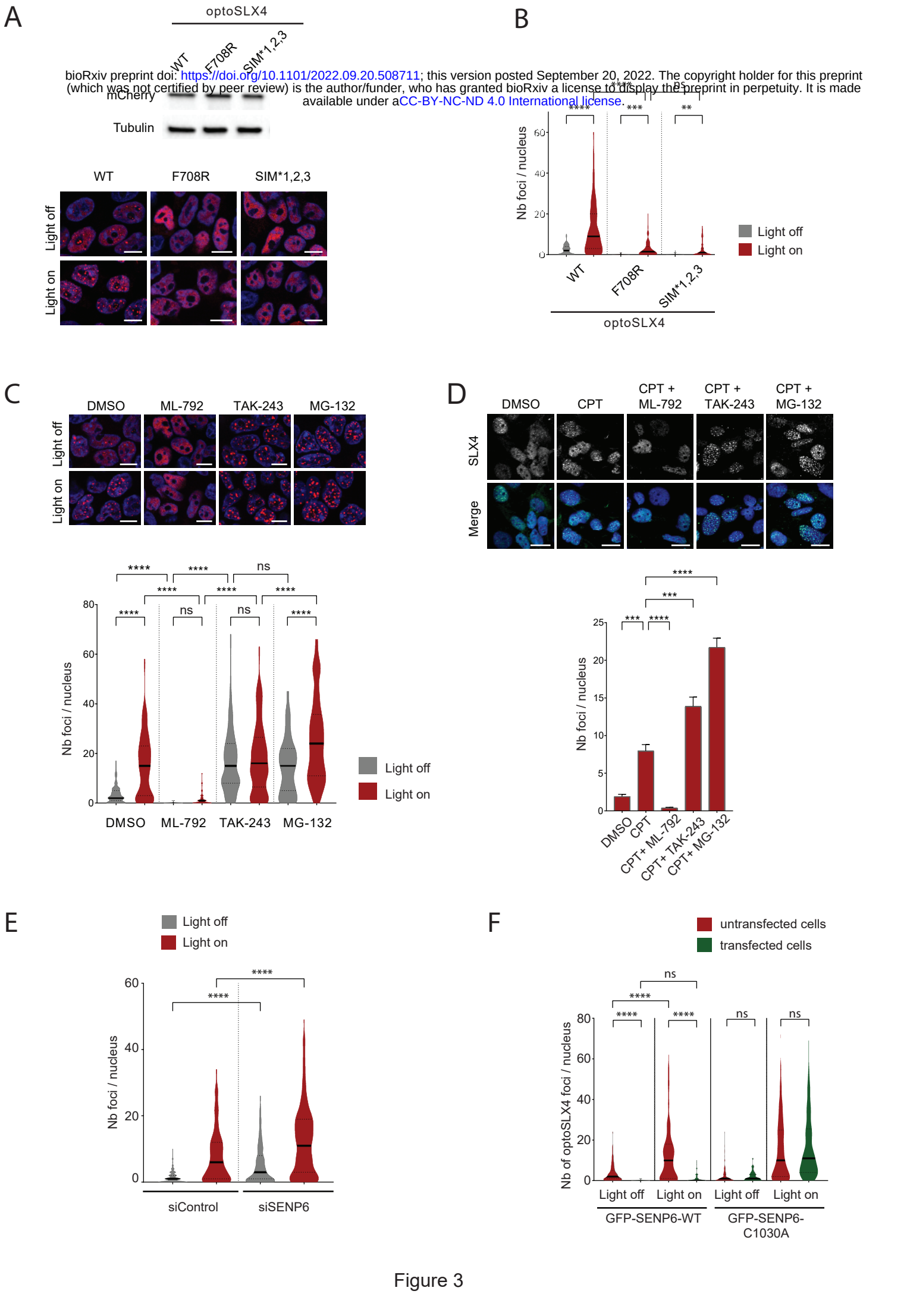

Figure 3

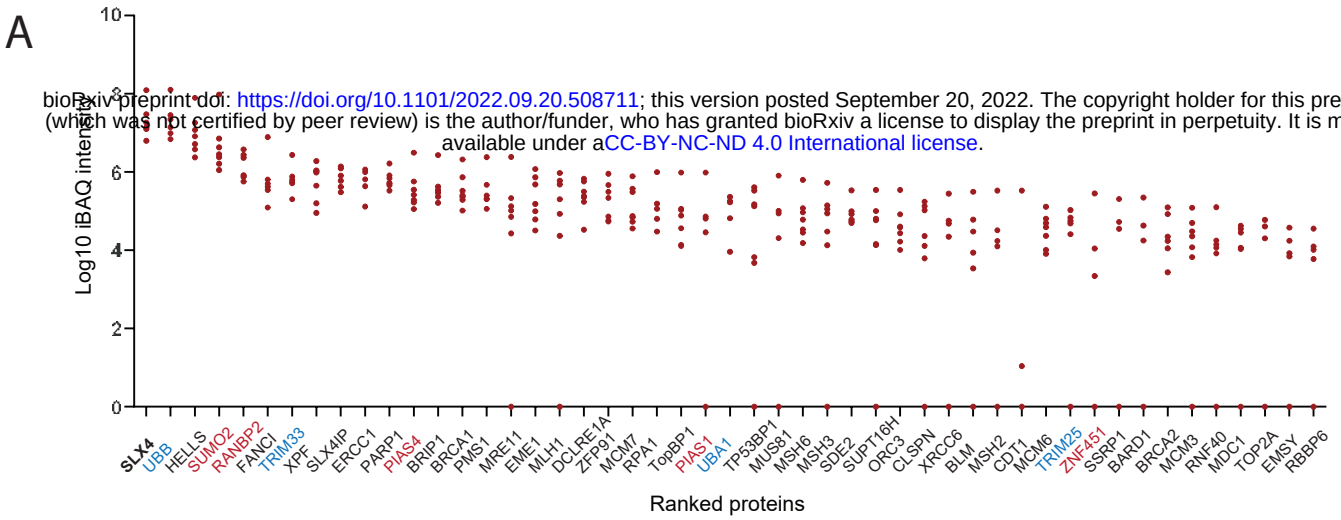

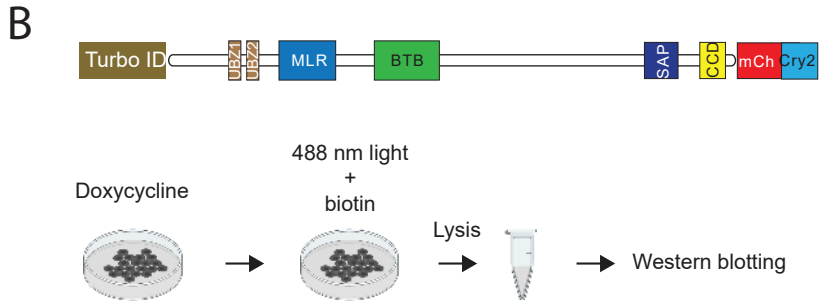

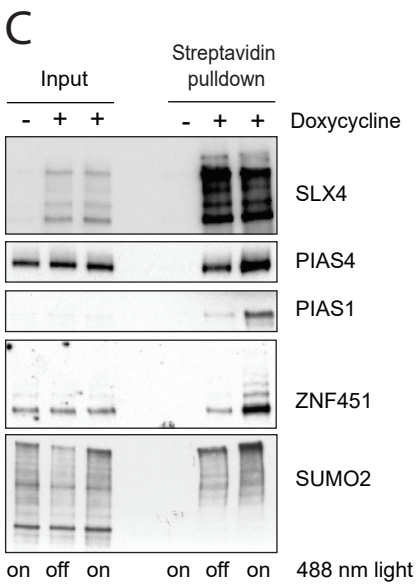

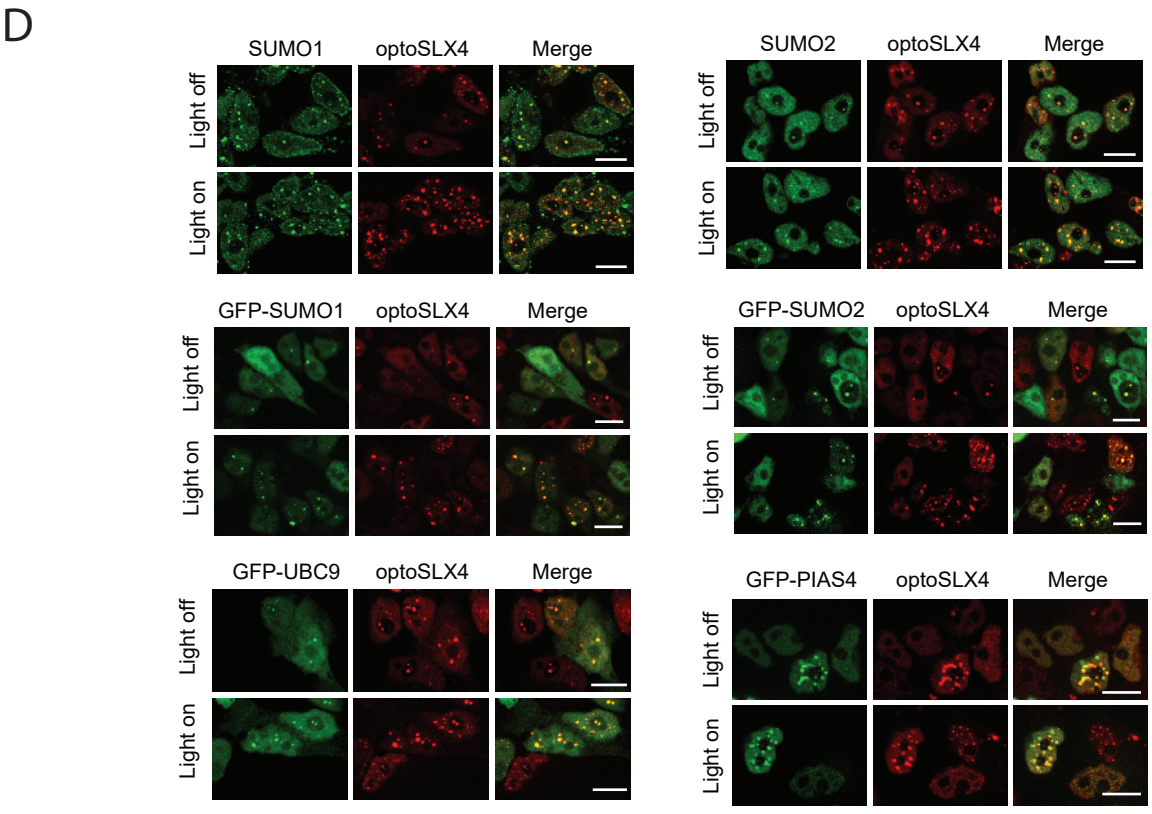

Figure 4

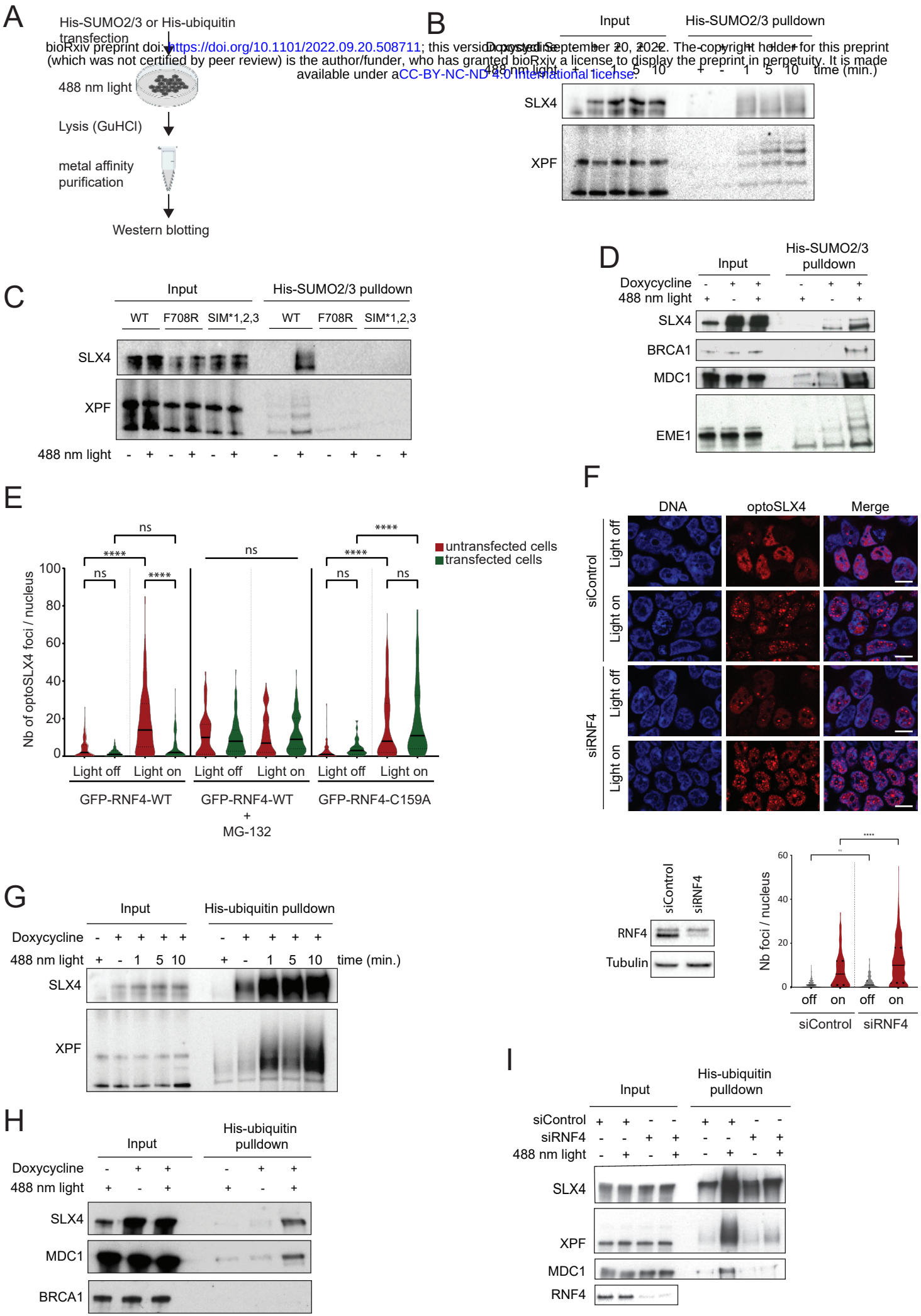

Figure 5

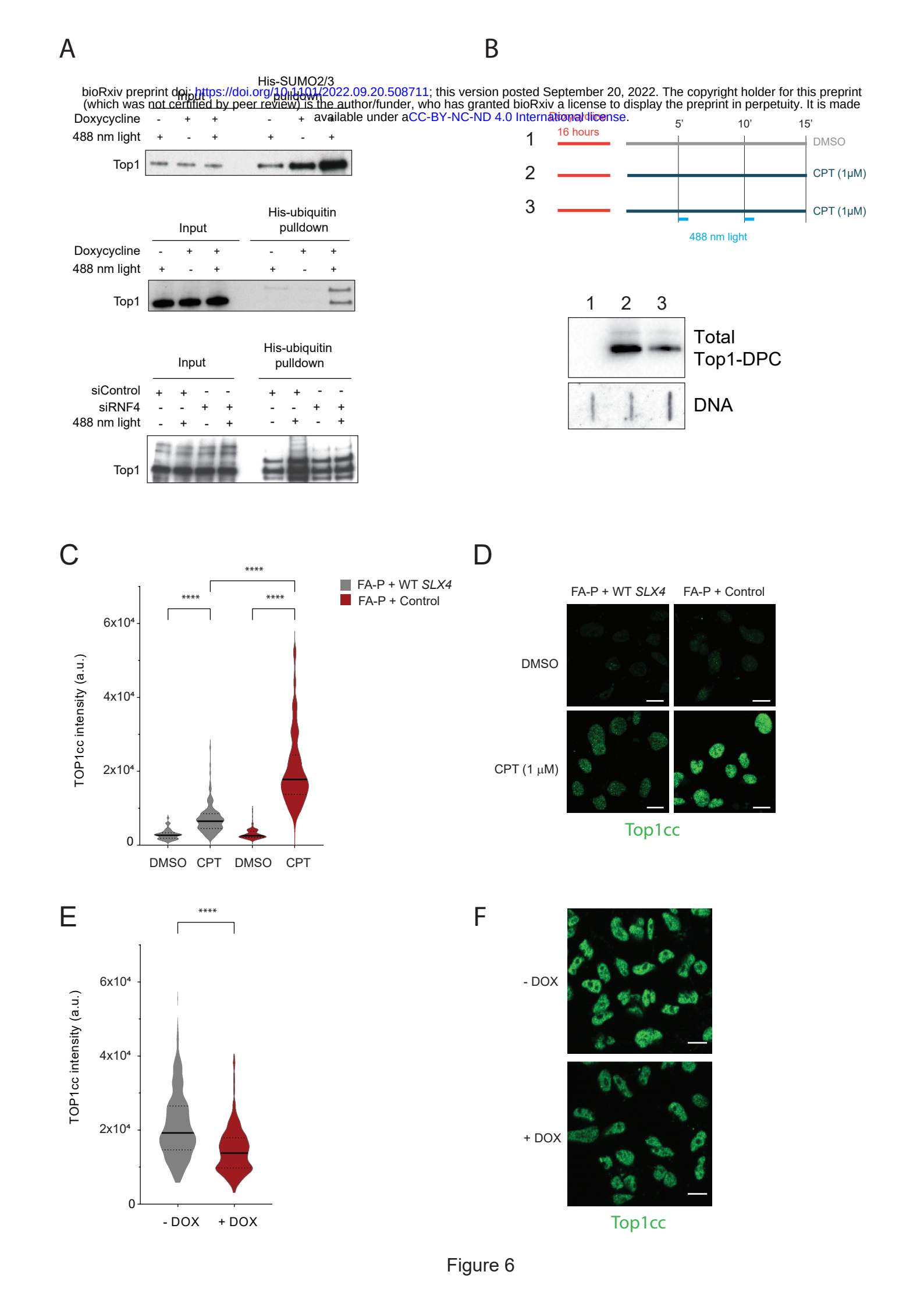

Figure 6

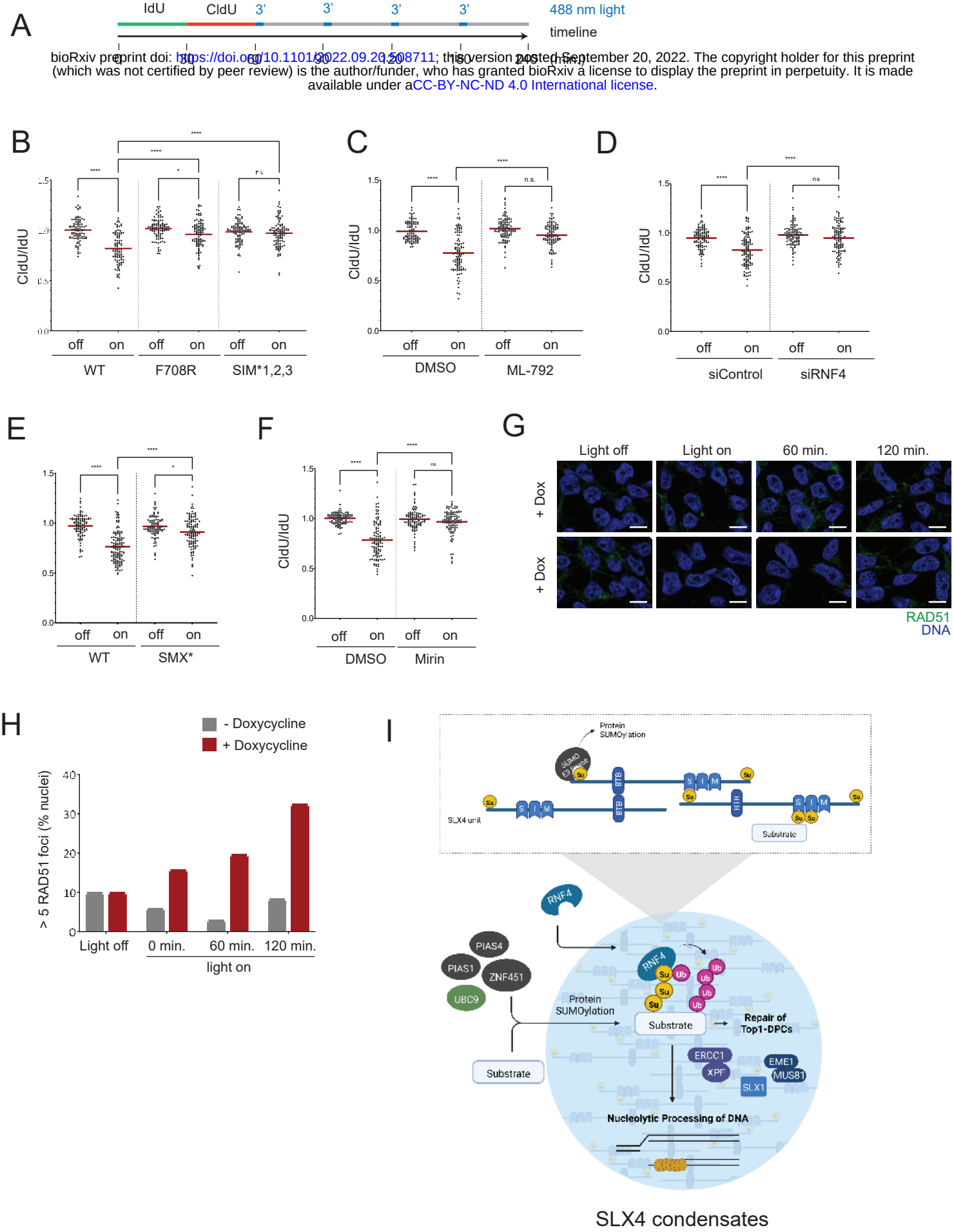

SLX4 condensates

Figure 7

A

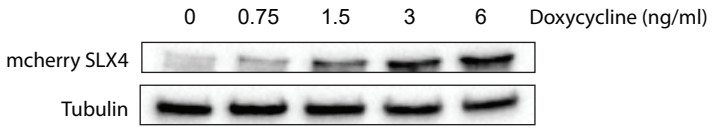

B

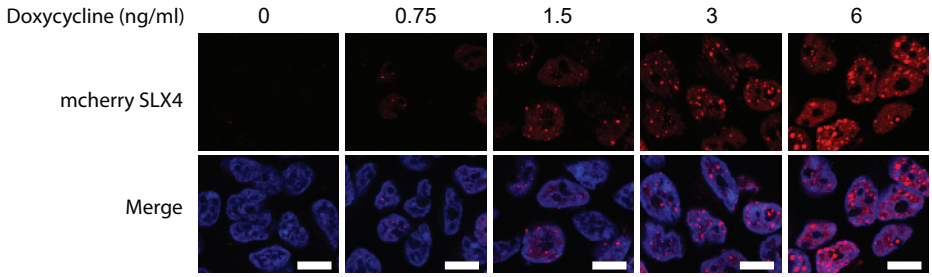

C

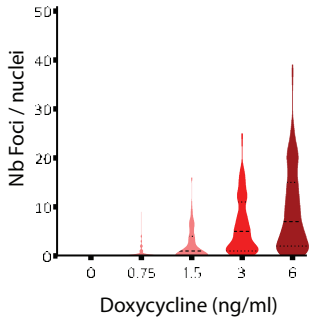

Figure S1

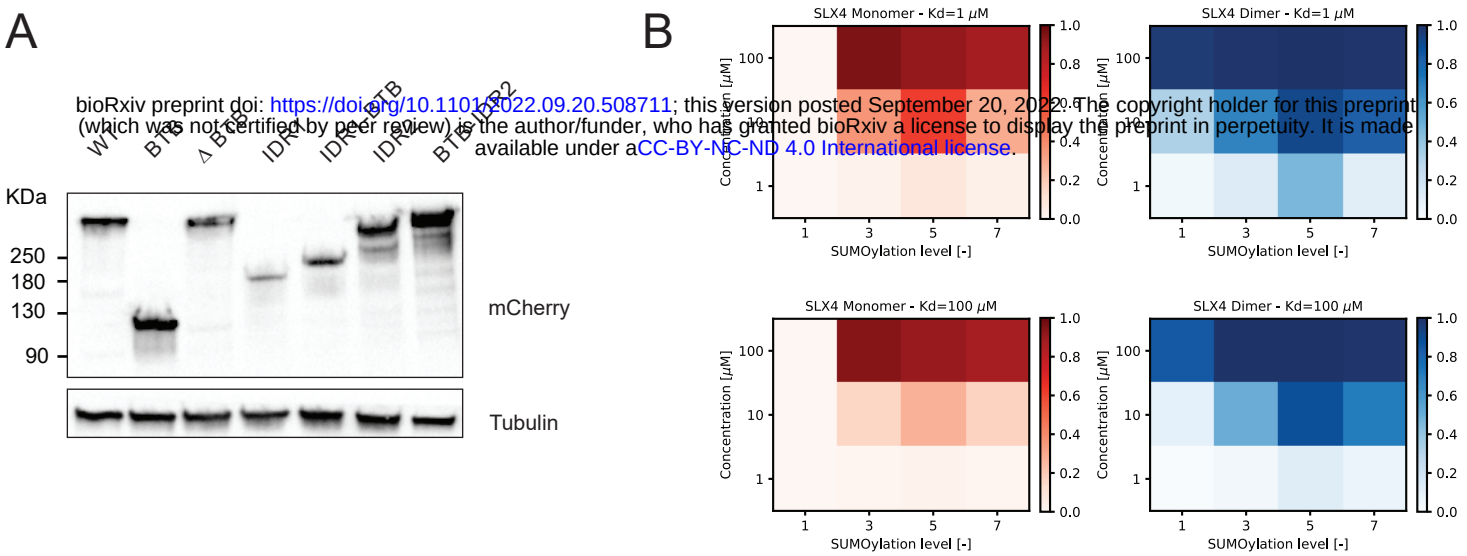

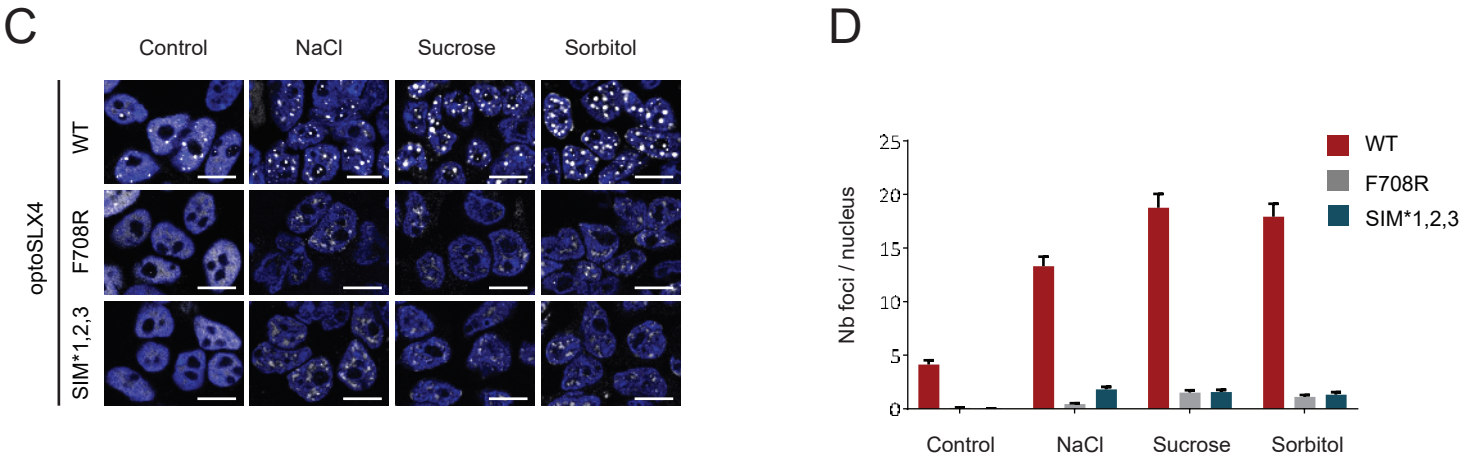

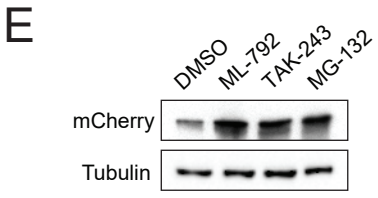

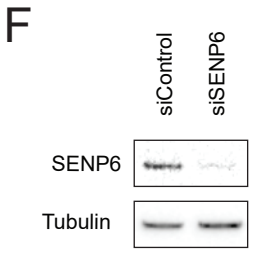

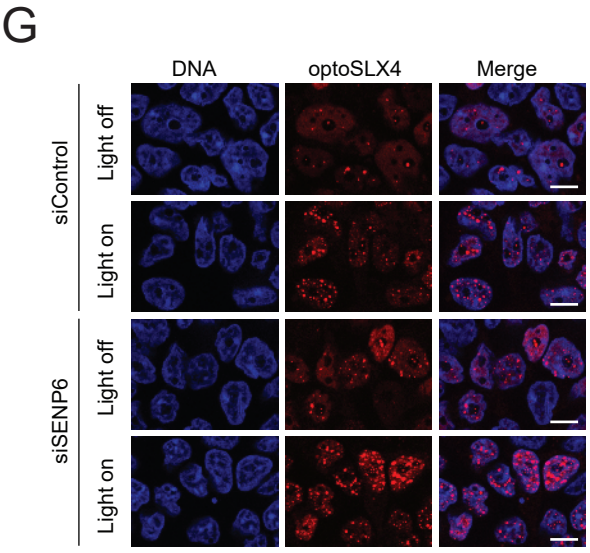

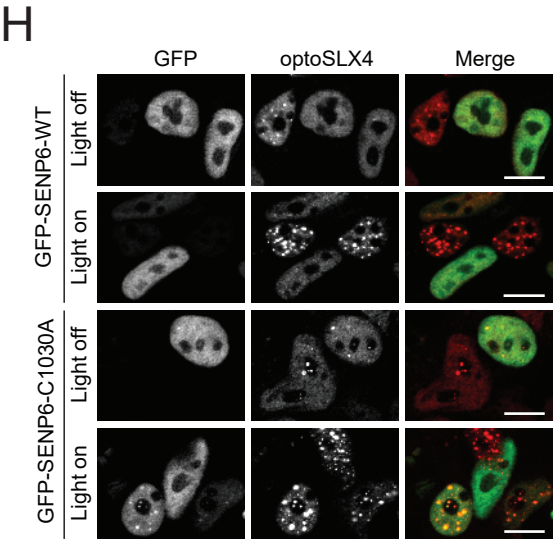

Figure S2

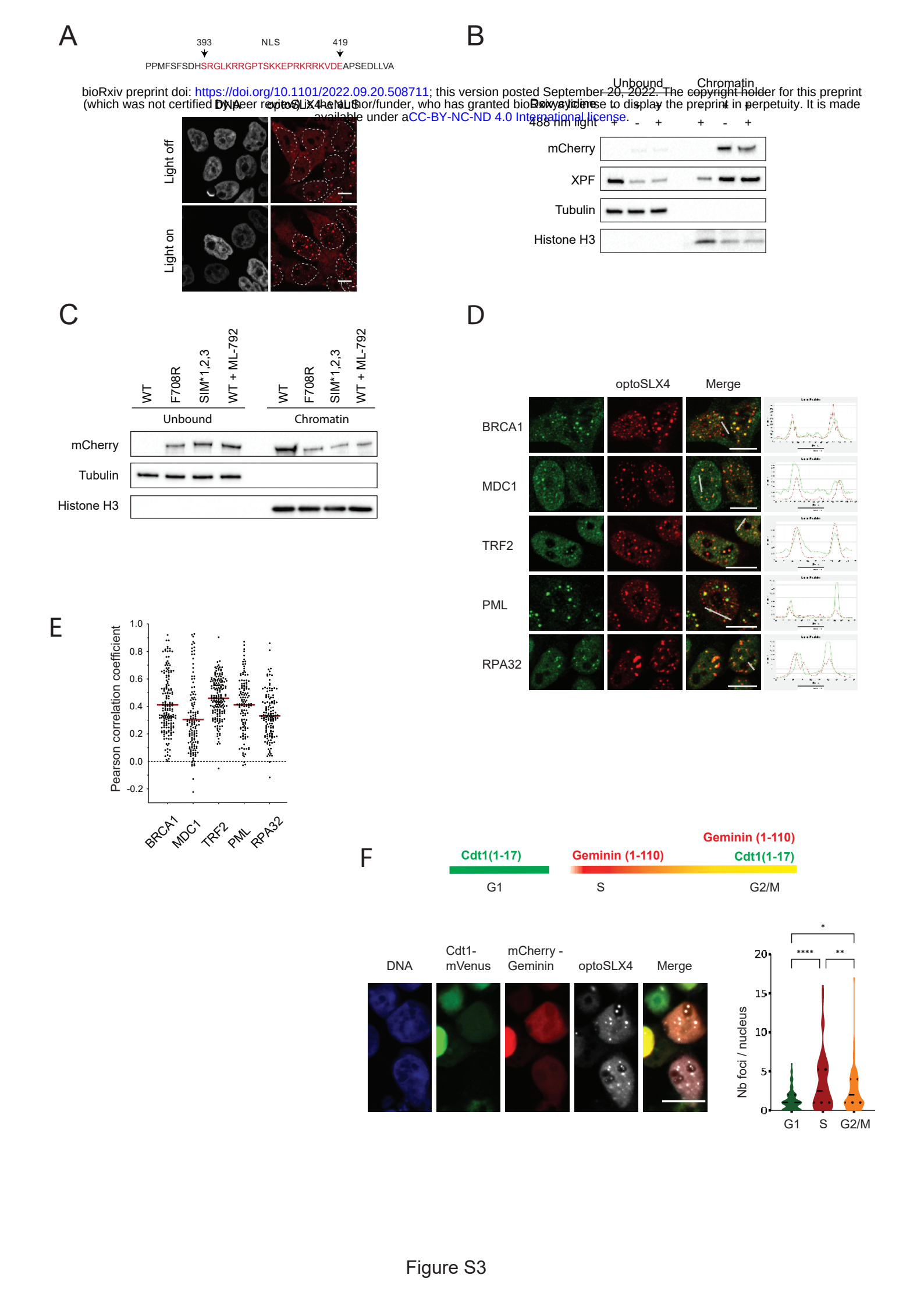

Figure S3

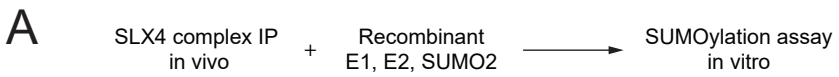

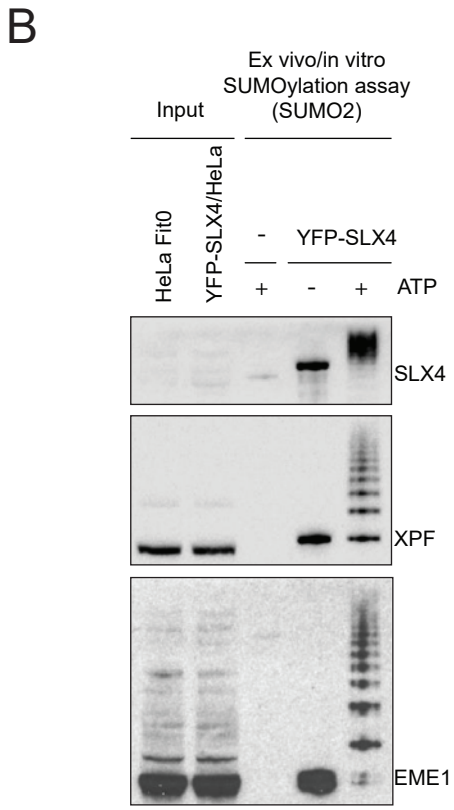

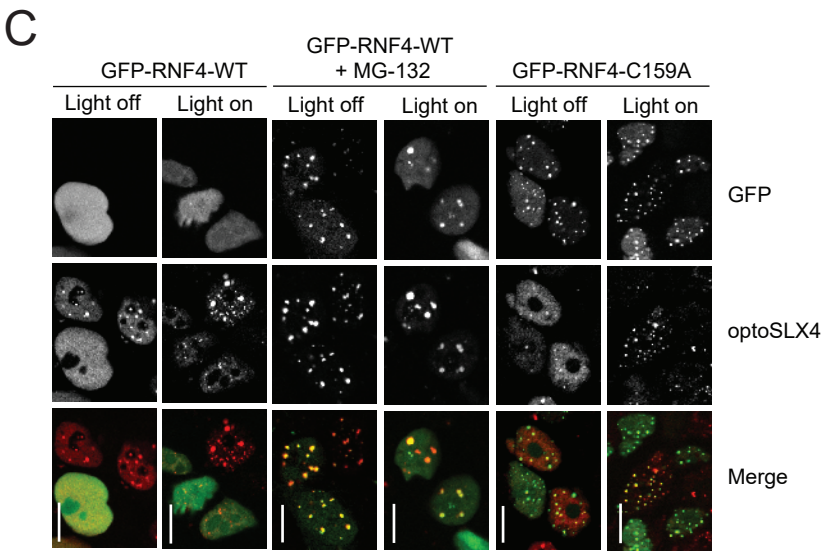

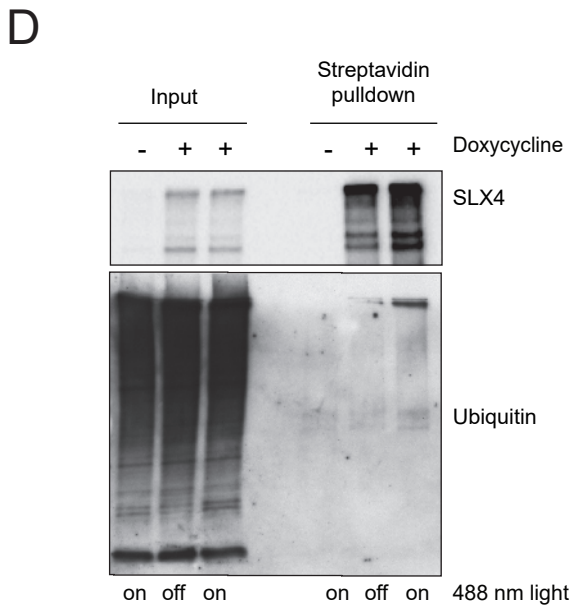

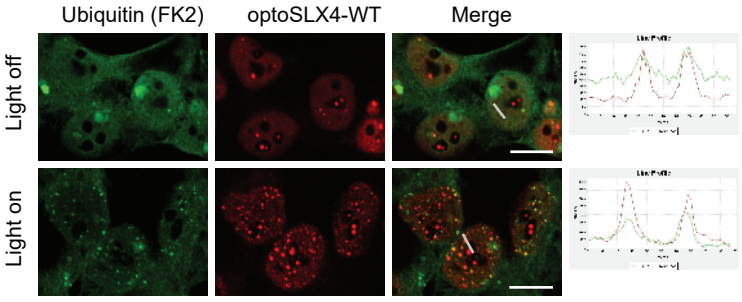

Figure S4

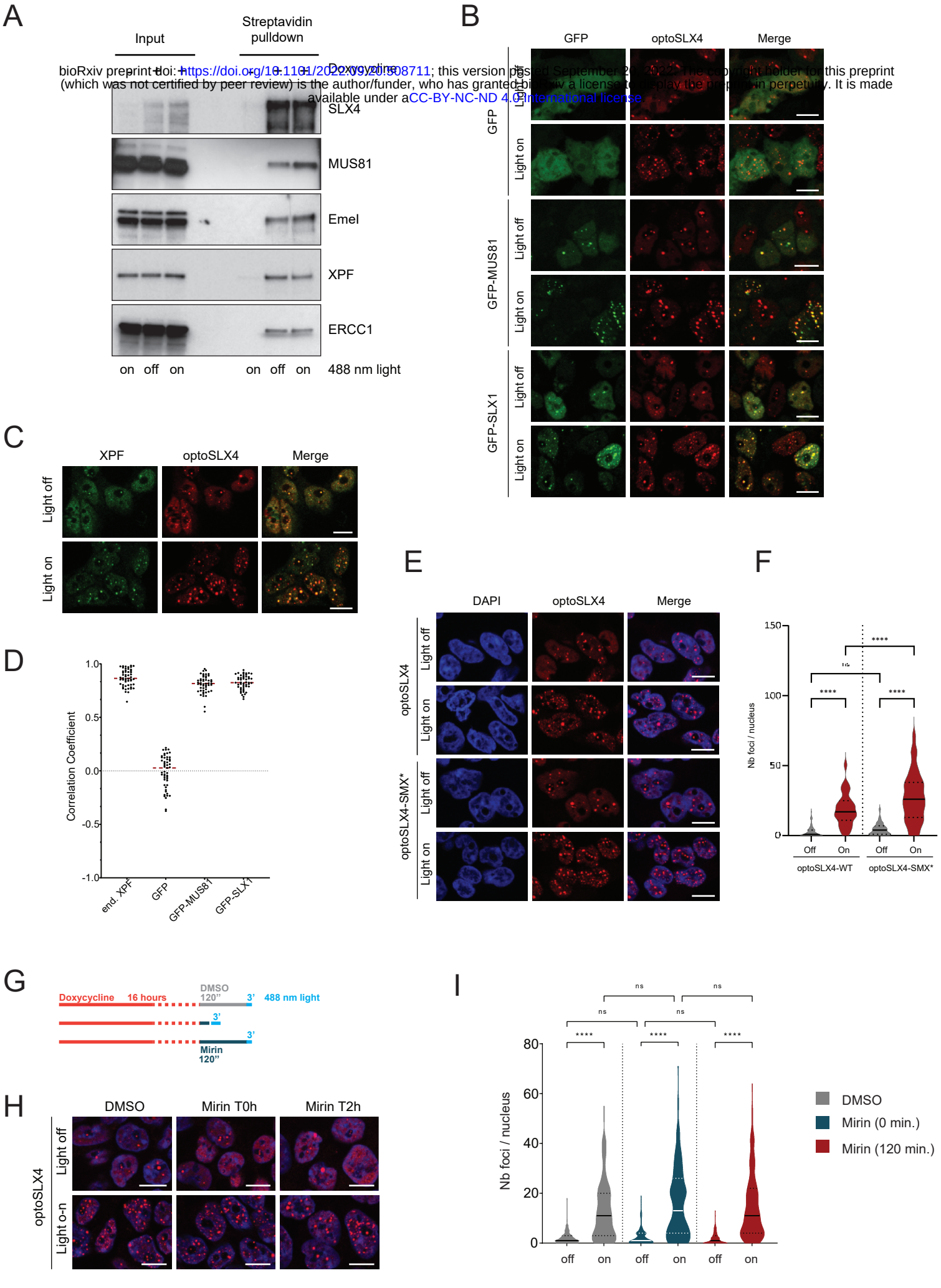

Figure S5